KINETIC PROPERTIES OF TRIPLE JUNCTIONS IN METALS STUDIED BY ATOMISTIC SIMULATIONS

By

QINGZHE SONG

A Thesis submitted to the Faculty of Graduate Studies of

University of Manitoba

In partial fulfillment of the requirement of the degree of

MASTER OF SCIENCE

Department of Mechanical Engineering

University of Manitoba

Winnipeg, MB

ABSTRACT

Nanocrystalline materials could exhibit high mechanical yield strength owning to its ultrafine grain configurations at nanometer level. Nevertheless, with a high volume fraction in nanocrystalline material, grain boundaries and triple junctions which store a relatively high free energy, are thermally instable which potentially contribute to grain growth by their migration and merging. On the other hand, since both grain boundaries and triple junctions are prior sites of impurity enrichment which could in return reduce the triple junction energy, alloys with impurity enriched in grain boundaries and triple junctions are widely applied to stabilize the nanostructures. However, past studies mainly focused on grain boundaries and the kinetic properties of triple junctions and their influences on the thermal stability of nanocrystalline metals is less studied.

In this work, triple junction mobility and impurity diffusivity in triple junction are studied by molecular dynamics simulations. Specifically, interface random walk method due to thermal fluctuation which has been widely applied to extract grain boundary mobility is extended to study triple junction motion. With this method, a new approach is developed to extract the intrinsic triple junction mobility. On the other hand, the impurity diffusion in three different types of triple junctions is investigated and all compared with the self-diffusion in triple junction and the adjacent grain boundary. It is found that the difference between impurity diffusion and self-diffusion is more significant in triple junction than that in grain boundary. In addition, self-diffusion at TJ and adjacent Σ5 (210) symmetric GB have identical diffusion properties. However, this conclusion cannot be applied to Σ5 (310) symmetric GB system and the inclined Σ5 GB system.

ACKNOWLEDGEMENTS

I would like to give my prior gratitude to my advisor, Dr. Chuang Deng, firstly for offering me this precious opportunity to pursue my post-graduate study in University of Manitoba. During my live and study here, I become much more organized and academically rigorous which owns to Dr. Deng's strict attitude and valuable advices. With his patient guidance, I gradually get familiar on my research and eventually could deal with academic problems independently. I felicitate myself on this treasurable research experience under such a knowledgeable professor.

Meanwhile, Prof. Francis Lin from Department of Physics, Prof. Olanrewaju Ojo and Prof. Chuang Deng from Department of Mechanical Engineering, I sincerely appreciate you being my committee members spending your precious time on reviewing my thesis and attending my defence.

I also want to express my gratitude to my parents. Thank you for your encouragement and support on my pursuing Master's degree. Both of us suffer the loneliness in the past two years and I really miss you. I always keep in mind that you spent much more time and concern on me than other parents. In the future, I desire to fight for a better life for my parents and me.

I am so fortunate that I meet my girlfriend here who deserves more than thanks from me. Your encouragement brings me confidence; your companion enlightened my life and let me to be a better man. I will work even harder, definitely taking responsibility of our future.

Last, I get a deep impression of the life in University of Manitoba. Professors who supervised my courses, students who shared our academic experience, staffs who helped me in my campus life, I would express my sincerely appreciation to everyone here.

TABLE OF CONTENTS

ABSTRACT ii

ACKNOWLEDGEMENTS iii

TABLE OF FIGURES vi

CHAPTER 1 MOTIVATION AND OBJECTIVES OF THIS WORK 1

1.1 Motivation 1

1.2 Objectives of This Work 3

CHAPTER 2 LITERATURE REVIEW 4

2.1 Grain Growth 4

2.2 Grain Boundary 4

2.3 Grain Boundary Mobility 6

2.3.1 Experimental 6

2.3.2 Molecular Dynamics Simulation 9

2.4 Triple Junction 14

2.5 Triple Junction Mobility 16

2.5.1 Analytical Models 17

2.5.2 Experimental 20

2.5.3 Molecular Dynamic Simulations 23

2.6 Grain Boundary Diffusion 26

2.7 Triple Junction Diffusion 28

2.8 Segregation 29

2.9 Impurity Diffusion in Grain Boundary 31

CHAPTER 3 METHODOLOGY 33

3.1 Molecular Dynamics Simulation 33

3.1.1 Canonical Ensemble (NVT) and Isothermal-isobaric Ensemble (NPT) 33

3.1.2 Embed Atom Method (EAM) Potential 34

3.1.3 Software 34

3.2 Models 35

3.2.1 The Model for Extracting TJ Mobility 35

3.2.2 The Model for Impurity Diffusion in Triple Junction 42

CHAPTER 4 RESULTS AND DISCUSSION 45

4.1 Triple Junction Mobility 45

4.1.1 Results from Method 1: Calculation from Individual GB Displacement (Order Parameter Involved) 45

4.1.2 Results from Method 2: Direct Detection of TJ Motion (Order Parameter Involved) 46

4.1.3 Results from Method 3: Calculation from the Average Position of Atoms in TJ Region (Ackland Parameter Involved) 47

4.1.4 Results from Method 4: Direct Detection of TJ Motion (Order Parameter and Ackland Parameter Involved) 48

4.2 Impurity Diffusion in Triple Junction 54

CHAPTER 5 SUMMARY 66

REFERENCE 68

TABLE OF FIGURES

Figure 2.1 Schematic models of (a) tilt and (b) twist boundaries between two ideal grains [18] 5

Figure 2.2 Dislocation configuration of a symmetrical ⟨100⟩ tilt low angle GB (LAGB) with a tilt angle θ[7] 5

Figure 2.3 Energy as a function of misorientation angle θ for GBs of silicon ferrite[19] 5

Figure 2.4 Coincidence site lattice (CSL) and structure of a 36.9˚⟨100⟩ tilt Σ5 GB in a cubic crystal lattice [7] 6

Figure 2.5 Schematic geometry of (a) Half-loop[24]and (b) quarter-loop[26]GB 8

Figure 2.6 Misorientation dependence of (a) the activation energy for GB migration and (b) the natural logarithm value of the pre-exponential factor of the reduced mobility [24] 9

Figure 2.7 The simulation cell in X-Y plane depicting the symmetrical U-shaped half loop GB (width *w* and misorientation angle 30˚). The bottom 3 layers of atoms are frozen at 0 K and the remaining atoms are thermostated to the desired temperature[11] 11

Figure 2.8 The time dependence of the area of U-shaped half-loop grain 2 as the GB migrates for the simulation depicted in Fig. 2.7 [11] 11

Figure 2.9 Schematic of the periodic computational cell used to extract GB mobility. The two fcc crystals C($n1$) and C($n2$) are misoriented by tilting ⟨111⟩ crystal direction equally to Y direction. The initial position of the GB (solid unshaded planes), the fluctuating profile h(**r**, t) (shaded planes) and computed average $h(t)$ (dotted, unshaded) are presented[8] 12

Figure 2.10 Distribution of the average interface position $h(t)$ at four time intervals 10ps, 20ps, 40ps and 80ps. Gaussian fits are shown[8] 12

Figure 2.11 Linear time dependence of the variance $\langle h2 \rangle$. Slope is the "diffusion coefficient"[8] ... 12

Figure 2.12 Different types of TJs consist with (a) three general GBs; (b)(c) mixed GBs and (d) three coincident (special) GBs[41] 14

Figure 2.13 Symmetric structure in TJ. Empty circle, solid circle and empty square represent atoms in three different grains solid line are the crystal planes (100), (110) and (010)[42] 15

Figure 2.14 Schematic description of Young-Dupre equation[42] 15

Figure 2.15 (a) Schematic description and (b) AFM geometry of TJ and adjacent GB grooves[44,45] 16

Figure 2.16 Geometry of the GB system with TJ during steady-state motion (a) $\theta < \pi 3$ (b) $\theta > \pi 3$ [49] 17

Figure 2.17 Schematic of expression $y = 2\cos\theta + 2\theta\sin\theta - 1$ in the first quadrant of the coordinate.....19

Figure 2.18 (a) GB system with TJ. Notches are to avoid the complete disappearance of the grain adjacent with GB I and GB Π; (b) the equilibrium system after annealing at 655˚C [49].....20

Figure 2.19 Temperature dependence of TJ (●) and GB (▲) mobility in (a) 21˚⟨111⟩ and (b) 21˚ ⟨110⟩ tilt GBs. Dotted line represents the mobility of a 21˚⟨111⟩ tilt GB in Al [7] (H=1.6 eV, A_0= 10^3 m^2/s)[49].....21

Figure 2.20 Half the dihedral angle θ as a function of Λ. (a) Geometry in Fig.2.16(a); (b) geometry in Fig.2.16(b) [3].....22

Figure 2.21 Reproducibility of measurement of the angle θ at five different temperatures[3].....22

Figure 2.22 Evolution of the shape of the GB system of a sample with symmetrical TJ with increasing temperature[3].....22

Figure 2.23 Temperature dependence of the criterion Λ for a symmetric TJ [3].....22

Figure 2.24 The area rate of shrinkage for 2-, 3-, 4-, 5-sided ($\beta < \pi/3$) grains as a function of critical inclination angle β. β increases with the TJ drag force[4].....23

Figure 2.25 Half-loop structure in (a) tri-crystal and (b) bi-crystal in MD simulation[46].....24

Figure 2.26 The dimensionless TJ mobility Λ as a function of the GB misorientation θ for w=25r_0 and T=0.125ε/*k* [46].....25

Figure 2.27 (a) The migration rate of TJ v_{tj} plotted as a function of the inverse of *w*[46] (b) The dimensionless TJ mobility plotted as a function of the grain width w[48].....25

Figure 2.28 (a) and (b) are the TJ migration simulation geometries in two opposite directions (+ and -). (c) is the geometries of bi-crystal model with same curved GB[48].....25

Figure 2.29 misorientation dependence of the TJ dimensionless mobility in the opposite direction compared with Figure 2.26[48].....26

Figure 2.30 Schematic shape of a penetration profile in the present of GB diffusion, c is the average concentration of the diffusion and y is the penetration depth [51].....27

Figure 2.31 The cylinder-like model to study self-diffusion in TJ. TJ and GB region are defined by black lines [40].....29

Figure 2.32 Arrhenius diagram of diffusion coefficients D calculated for the TJ, Σ5 GB, general GB, and liquid cooper. Experimental results for self-diffusion are shown for comparison [40].....29

Figure 2.33 D_{gb} in nanocrystalline materials without TJs (◦) and with TJs (●).....29

Figure 2.34 Nickel diffusion in the GB and TJ in Copper crystalline materials at different times[58] 30

Figure 2.35 (a) Ni concentration (brightness related) in GBs and TJ at a series piece of slices perpendicular to TJ line (b) Ni concentration distribution in the GB[58] 30

Figure 2.36 Concentration profile along the Σ5 GB with a TJ at the end[47] 31

Figure 2.37 Product of GB velocity and temperature as a function of the reserve temperature[61] .. 32

Figure 2.38 Arrhenius plots of impurity diffusions and self-diffusion in Ag GB[51] 32

Figure 3.1 The simple description of the MD simulation algorithm 33

Figure 3.2 the honeycomb-shape cell in our simulation using Atomeye software. (a) Ackland parameter involved which distinguish the non-FCC atoms in interfaces from FCC atoms in the crystals. (b) Order parameter involved which distinguish atoms in different crystal grains with different orientations 36

Figure 3.3 A schematic description of method 1. (a) The TJ region and three adjacent GBs; different colors represent different grains. Rectangles are three defined regions across these GBs to calculate the migration of GBs. (b) The schematic description of (a); solid lines are GBs initially and dash lines are their positions after simulation for a time period Δt. "*d*" with different subscripts indicate the displacement of TJ and GBs. Blue region in the rectangle is a group of atoms with one reference orientation and red is another group of atoms with the other reference orientation. Purple represents the atoms initially belong to reference 1 and after Δt belong to reference 0. 38

Figure 3.4 A schematic description of method 2. (a) The TJ region with three adjacent GBs; order parameter is involved. One grain is set as reference 0 while the other two grains are set as reference 1. White rectangular region is defined to calculate the TJ displacement in the horizontal direction. (b) The schematic description of (a); A and B are the length and width of the defined region. x is the height of the triangular shape in which atoms have an order parameter 0. X_0 is the TJ displacement in horizontal direction 39

Figure 3.5 A local configuration of the TJ with Ackland parameter involved. Dash line indicates the positions of non-FCC atoms in two general GBs; solid line indicates the average position of these non-FCC atoms in z direction as well as the non-FCC atoms in the Σ5 GB which is along z direction. So the total average position of all non-FCC atoms in this region could represent the displacement of TJ in z direction 41

Figure 3.6 A schematic description of method 4. (a) A circular region with radius of 12Å sweeps in the x-z plane across TJ (order parameter involved). N1, N2 and N3 are the amount of atoms in this region belonging to Grain 1, Grain 2 and Grain 3, respectively. (b) N^2 calculated from Eq.

3.9 plotted in X-Z plane landscape. (c) The logarithm value of N^2 in X-Z plane landscape. (d) The view from bottom of (c) 42

Figure 3.7 (a) A 3D cylinder model to extract the diffusion of impurity atoms in TJ. Radius is 6 nm and the length is 8 nm. A Σ5 GB (Σ5(310)[001] tilt GB in figure) is built horizontally. The circular and rectangular purple regions are defined as TJ and GB regions, respectively (b) Bi-crystal model with a specific GB (same type, same size with that in tri-crystal model) in center 44

Figure 4.1 (a),(b) and (c) are the three GBs displacements in 16 random walks. (d),(e) and (f) are their corresponding mean square displacements (in Method 1) 45

Figure 4.2 (a), (b) and (c) are TJ displacements along three GBs in 16 random walks. (d),(e) and (f) are their corresponding mean square displacements (in Method 2) 46

Figure 4.3 (a),(b) and (c) are TJ displacements in three directions perpendicular to each GB. (d),(e) and (f) are their corresponding mean square displacements (in Method 3) 48

Figure 4.4 (a) and (b) are TJ displacements in X and Z direction. (c) and (d) are their corresponding mean square displacements (in Method 4) 49

Figure 4.5 Time dependence of the mean square radius r^2 extracted from four methods (a), (b), (c) and (d), respectively. The slopes of linear fitting are the TJ "diffusion coefficient" D in Eq. 3.3. The correlation factor R^2 are shown which indicates the goodness of the linear fitting. 50

Figure 4.6 Adapted diagram from Figure 4.5(d) method 4 52

Figure 4.7 (a) Time dependence of the mean square displacement of Σ5 (310) tilt symmetric GB in both bi-crystal and tri-crystal model (b) Σ5 (310 GB displacements in bi-crystal model 53

Figure 4.8 Mean square TJ displacements in Z (a~d) and X (e~h) directions extracted from method 1 (a),(e), method 2 (b),(f), method 3 (c),(g), method 4 (d),(h) 54

Figure 4.9 Impurity MSDs in X(a), Y(b), Z(c) directions in the TJ with a Σ5 (310)[001] tilt symmetric GB adjacent in pure Aluminum system at 700K 54

Figure 4.10 Time dependence of the impurity mean square displacements in TJ with different concentrations (number of impurity atoms) at 650K 55

Figure 4.11 Time dependence of the impurity mean square displacement in TJ at a series of temperatures 55

Figure 4.12 Temperature dependence of diffusion coefficients in natural logarithm coordinate along (Y in red) and across (X in green and Z in yellow) the TJ. The slope is their diffusion activation energy which are summarized in Table 4.1 57

Figure 4.13 (a), (b), (c) are mean square displacements of the atoms in both TJ and ∑5 (310) tilt GB (parallel-Y and perpendicular-X to the tilt axis) in pure Al system in a range of 550K to 700K. (d)The natural logarithm value of these diffusion coefficient verse 1/kT. The activation energy are presented in (d)..... 60

Figure 4.14 Temperature dependence of the self-diffusion coefficients in both x and y directions in symmetric ∑5(210), ∑5(310) and inclined ∑5 GBs. 61

Figure 4.15 Time dependence of mean square displacements (a) of different concentrations of Ni impurities in the TJ with ∑5 (210)[001] tilt symmetric GB adjacent at 650K and (b) at a series of temperature from 550K to 800K. Curvature at 650K is the average of MSD in (a)..... 62

Figure 4.16 Time dependence of mean square displacements (a) of different concentrations of Ni impurities in the TJ with inclined ∑5 GB adjacent at 650K and (b) at a series of temperature from 550K to 725K. Curvature at 650K is the average of MSD in (a). The TJ structure crashed at above 750K which is then not included 62

Figure 4.17 Temperature dependence of natural logarithm values of the diffusion coefficients for diffusion along TJ (Y, green), diffusion parallel to GB tilt axis (Y, red) and diffusion perpendicular to GB tilt axis (X, black) in (a) system with a ∑5 (210)[001] tilt symmetric GB, (b) system with an inclined ∑5 GB..... 63

Figure 4.18 The natural logarithm values of the diffusion coefficients for the impurity diffusion along TJ with inclined ∑5, ∑5 (210)[001] tilt symmetric and ∑5 (310)[001] tilt symmetric GBs adjacent, respectively..... 64

Figure 4.19 Comparison of self-diffusion and impurity diffusion both in inclined ∑5 GB and TJ with the same GB adjacent. Full red triangle data is from H. Sun[73] 65

CHAPTER 1 MOTIVATION AND OBJECTIVES OF THIS WORK

1.1 Motivation

Grain boundaries (GBs) are interfaces that separate two grains with identical structures but different orientations in polycrystalline materials. Triple junctions (TJs) are where three GBs meet. Owning to their disordered crystal structure and high surface tension, GBs and TJs have a relatively higher free energy than that of grains and therefore thermally instable which potentially contribute to grain growth and recrystallization[1] in polycrystalline materials by their migration, merging, sliding and interaction either mutually or with crystal dislocations. It was assumed previously by Mullins[2] that TJs have a minor importance on the GB motion and TJs in crystalline materials only maintains the thermodynamic equilibrium by fixing dihedral angles during GB migration. However, recent studies [3,4] reported a finite value of TJ mobility which means that the TJ could have a mutual interaction with GBs and involve additional energy dissipation during GB migration process. Particularly when the grain size is reduced to nanoscale (<100nm), the volume fraction of GBs and TJs will increase dramatically. In this case, GBs and TJs could significantly influence the thermal stability of the nanocrystalline materials which could lead to grain growth even at ambient temperature[5]. However, while GB motion has been extensively studied in the past, the influences of TJs on the thermal stability of nanocrystalline materials are still not well addressed.

The mobility and diffusivity are two essential parameters to characterize the kinetic properties of TJs. Specifically, the TJ mobility could be used to estimate TJ migration, the grain growth and help to identify whether TJ has a drag effect on GB motion[4]. Thus, the TJ mobility is of great importance to study the role of TJs on grain growth especially in nanocrystalline materials. On

the other hand, TJs are a fast diffusion path in materials and TJ diffusion is essential for phase transformation which could eventually lead to materials degradation[6]. Especially in nanocrystalline materials, the overall mass transportation may be dominated by TJ diffusion. Moreover, TJ diffusivity has a deep correlation with the TJ mobility which has been previously observed[7].

Due to the difficulties in fabricating ultra-pure samples with desired GBs or TJs and detecting the migration of GBs or TJs in experiments, molecular dynamics (MD) simulations have been widely applied to study GB and TJ motion. To date, in most research on GB and TJ motion from MD simulations, an applied driving force is involved based on the assumption that $v=M \bullet P$ where v is the GB or TJ velocity, M is the mobility and P is driving force. However, this applied driving force could influence the underlying mechanism and as a result the intrinsic mobility cannot be extracted properly[8]. Thus, thermal fluctuation, which has been proved[8] to successfully extract GB mobility without the need of an applied driving force, is applied in this work to extract the TJ mobility. On the other hand, it is important to study the effect of impurities on TJ mobility in order to evaluate its influence on TJ thermal stability. However, it is suspected that the thermal fluctuation of TJs with segregated impurities would become too subtle to be accurately detected in MD simulation. Therefore, since a deep correlation has been found between GB migration and diffusion[9,10], instead of focusing the TJ mobility with impurities directly, the impurity diffusion in TJ is used as an indirect but easier way to evaluate the influence of impurities on the TJ motion.

1.2 Objectives of This Work

1. Develop a method to extract the intrinsic TJ mobility by MD simulations based on interface random walk (IRWalk) method.

2. Extract the diffusivity and activation energy for the impurity diffusion in TJ with Σ5 GB adjacent.

3. Compare the TJs (adjacent with Σ5 GBs) migration and diffusion mechanisms with those of Σ5 GBs.

CHAPTER 2 LITERATURE REVIEW

2.1 Grain Growth

Grain growth is a common phenomenon in polycrystalline materials owning to the GB migration and merging[11–14]. The excess free energy of GB, or in other words, the surface tension of GB is the driving force of grain growth since grain growth could lead to a decrease in GB surface area thus a reduction in the free energy[7]. During this process, some grains will shrink while others will grow but on average the mean grain size will increase. Such a change in microstructure of crystalline materials could significantly affect some mechanical properties like yield stress and potentially play a role in conductivity and chemical oxidization.

The relation between grain size and yield strength could be mathematically illustrated by Hall-Petch Equation[15,16]:

$$\sigma_y = \sigma_0 + \frac{ky}{\sqrt{d}} \tag{2.1}$$

where σ_y is the yield stress, σ_0 is a constant for the starting stress, ky is the strengthening coefficient and d is the average grain size.

In order to maintain the grain size in a nanoscale to achieve these beneficial properties including high yield strength and ideal surface catalytic activity[17], grain growth should be prevented effectively. Before that, TJ migration mechanism needs to be investigated as clearly as GB migration which has already been extensively studied in previous works.

2.2 Grain Boundary

GB is a two-dimensional defect in crystalline materials separating two adjacent grains with different orientations. Atoms in GB region merely occupy crystal site thus the structure of GB is much more open and disordered than that of ideal crystals.

GB could be generally classified as twist GB (the twist axis perpendicular to the boundary plane) and tilt GB (the tilt axis parallel to the boundary plane) shown in Figure 2.1.

This image has been removed due to copyright issues. Please refer to its source.

Figure 2.1 Schematic models of (a) tilt and (b) twist boundaries between two ideal grains [18]

The misorientation angle of a tilt GB could highly influent the GB energy and other properties. When the angle is less than 15 degrees, GB which is entirely consisted with isolate and periodic dislocations is called low angle GB (LAGB) (see Figure 2.2).

This image has been removed due to copyright issues. Please refer to its source.

Figure 2.2 Dislocation configuration of a symmetrical ⟨100⟩ tilt low angle GB (LAGB) with a tilt angle θ[7]

In contrast, high angle GB (HAGB) has a misorientation angle larger than 15 degrees. The structure is considerably more disordered and has a relatively higher surface energy than LAGB. HAGB energy is observed experimentally to be independent with misorientation angle[19] while LAGB energy mentioned above is correlated with misorientation. Both the HAGB energy and LAGB energy are plotted with misorientation in Figure 2.3. However, there are some HAGBs with specific misorientation angles whose interfacial energies are significantly lower than those general HAGBs. Those are defined as CSL[20] (coincidence site lattice) model.

This image has been removed due to copyright issues. Please refer to its source.

Figure 2.3 Energy as a function of misorientation angle θ for GBs of silicon ferrite[19]

Figure 2.4 is a simple example of CSL model[7]. The ⟨100⟩ axes of both adjacent lattices have a rotation angle of 36.87°. If the periodic atomic arrangements of the adjacent lattices are extended to the other side of the symmetric GB, there could be some sites overlapped periodically. These periodic coincidence sites define another lattice which is called coincidence site lattice. The new lattice has a larger lattice constant than the original one and such a HAGB could be defined by measuring the density of coincidence site:

$$\Sigma = \frac{volume\ elementary\ cell\ of\ CSL}{volume\ elementary\ cell\ of\ crystal\ lattice} \tag{2.2}$$

The value of Σ in Figure 2.4 is$\Sigma = \frac{a(a\sqrt{5})^2}{a^3} = 5$, thus the HAGB is defined as $\Sigma 5$ symmetric GB. It is apparent that a lower value of Σ results in a more finely ordered and stable GB structure.

This image has been removed due to copyright issues. Please refer to its source.

Figure 2.4 Coincidence site lattice (CSL) and structure of a 36.9°⟨100⟩ tilt Σ5 GB in a cubic crystal lattice [7]

2.3 Grain Boundary Mobility

2.3.1 Experimental

Due to high surface energy, GBs tend to migrate to minimize the surface energy and reach an equilibrium thermal dynamic state. The process[7] of GB motion is assumed that the atom detaching one grain to join in the other grain ruins a crystal site rather than creating a vacancy and attaching to the adjacent grain generates a new crystal site rather than fill in a vacancy. Based on different frame references, GB motion is only mathematically treated as atoms jump across the GB. In this case, the velocity of an atom cross the narrow GB is simply[7]:

$$v = b(\Gamma_+ - \Gamma_-) \tag{2.3}$$

Γ_+ and Γ_- are the jump frequency of atoms from one crystal to the other. Symbol "+" and "-" represent two opposite jump directions. b is the burgers vector. If $\Gamma_+ = \Gamma_-$ which means there is no Gibbs free energy difference between the adjacent grain, velocity will equal to zero and GB won't move. If the net flux is non-zero, the driving force P is:

$$P = -\frac{dG}{dV} \tag{2.4}$$

V is the one atomic volume which is approximately b^3, thus,

$$v = b\left(\nu_{\mathrm{D}} e^{-\frac{G_{\mathrm{m}}}{kT}} - \nu_{\mathrm{D}} e^{-\frac{G_{\mathrm{m}}-Pb^3}{kT}}\right) = b\nu_{\mathrm{D}} e^{-\frac{G_{\mathrm{m}}}{kT}}\left(1 - e^{-\frac{Pb^3}{kT}}\right) \tag{2.5}$$

The frequency $\nu^+ = \nu^- = \nu \approx \nu_D$ (Debye frequency) and G_{m} is the migration free energy in both directions. For all practical cases $PV \ll kT$, thus $e^{-\frac{Pb^3}{kT}} \cong 1 - \frac{Pb^3}{kT}$,

$$v = \frac{b^4 \nu_{\mathrm{D}}}{kT} e^{-\frac{G_m}{kT}} \cdot P \equiv M \cdot P \tag{2.6}$$

M refers to the mobility. From this equation the mobility M could be concluded as a parameter dependence only on Temperature and GB type (G_m) rather than the applied driving force (P) and in hence was experimentally verified[21]. As a thermal dynamic property, mobility obeys Arrhenius equation[22]:

$$M = M_0 \cdot \exp(-\frac{Q}{kT}) \tag{2.7}$$

where M_0 is a pre-exponential factor, Q is the activation energy, k refers to Boltzmann constant and T is the temperature.

The driving force could be applied in various ways on GBs. The advantages and disadvantages are listed in Table 2.1.

This table has been removed due to copyright issues. Please refer to its source.

Table 2.1 different types of driving forces applied on GB migration in crystalline materials as well as their advantages and disadvantages[7]

Among all these driving forces applied to study the GB motion, driving force generated from GB energy is the most popular one. Advantages of such a driving force over the others are mainly two points: (1) GB energy as a source of driving force is usually generated from a curved GB which is almost everywhere in crystal materials, thus no external effort is needed to construct the samples. (2) The magnitude of such a driving force generated from a curved boundary is not too large so that the observation on GB motion is continuously accessible.

Half-loop GBs and quarter-loop GBs (see Figure 2.5) are widely used in studying GB migration. Dr. Gottstein[24] and his co-workers build a half-loop pure Aluminum ⟨111⟩ tilt GB assuming that the half-loop shape is in a steady-state shape during GB migration(Figure 2.5(a)). The rate of change of area of the shrink grain could be extracted by:

$$\dot{A} = vw = (M\gamma\boldsymbol{\kappa})w \tag{2.8}$$

where M is GB mobility, γ is GB energy per unit area, $\boldsymbol{\kappa}$ is the curvature and w is the width of half-loop shape, $\boldsymbol{\kappa} = \frac{\mathbf{2}}{\boldsymbol{w}}$.

This image has been removed due to copyright issues. Please refer to its source.

Figure 2.5 Schematic geometry of (a) Half-loop[24]and (b) quarter-loop[26]GB

Since γ is not a thermally independent parameter, $(M\gamma)$ as a combine rather than the intrinsic mobility M could be extracted, which is represented by M^* namely "reduced mobility".

$$\dot{A} = vw = (M\gamma\boldsymbol{\kappa})w = 2M\gamma \tag{2.9}$$

Thus the rate of changing area could be linearly related with GB reduced mobility. By simply measuring the area change with time, they get the reduced mobility at different temperatures, with different orientations and different curvatures. This method is also similarly applied to extract the TJ mobility which will be introduced in details later on.

Along with other studies, GB migration is mainly concluded as:

(1) Strongly dependent on misorientation[14,21,24,27](Figure 2.6). When the tilt angle is near 40.5°, both activation energy and mobility reach to maximum value[24,27].

(2) With identical tilt angle, the activation energy and mobility also varied with the ways two crystals tilt to each other[30]. Normally a symmetric tilt GB has a lower activation energy and mobility than an asymmetric tilt GB.

(3) GB migration in transverse direction differing from that in longitudinal direction indicates an anisotropic activation energy and mobility. [31]

(4) Different dopant atoms have different influence on GB migration. [23]

This image has been removed due to copyright issues. Please refer to its source.

Figure 2.6 Misorientation dependence of (a) the activation energy for GB migration and (b) the natural logarithm value of the pre-exponential factor of the reduced mobility [24]

2.3.2 Molecular Dynamics Simulation

Although experimental approach could extract GB mobility accurately and reliably, the essential drawback is that a specific type of GB with a certain tilt angle and misorientation is very difficult to fabricate and control thus the GBs taking into consideration are narrowly limited. To avoid it,

MD simulation[32] is developed which could study interface migration with a wider range of continuous misorientation angles.

MD simulation is a computer simulation of physical movements of interactive atoms and molecules in a period of time. The atomic physical movements are determined by numerically solving the Newton's equation of motion for a system of interacting particles where forces between atoms and potential energy are defined by molecular mechanics force fields [33].

Previous simulation methods based on MD can be grouped into two different categories: applied driving force method and thermal fluctuation method.

2.3.2.1 Applied Driving Force

Generally an applied driving force is needed for GBs or TJs migration by using this method. As similar to experimental method, a curved GB is constructed to generate the driving force in many studies[11,24,34].

For example, Dr. Upmanyu[11] studied the relationship between GB mobility and temperature. Their two dimensional model is present in Figure 2.7, a half-loop shape GB with width *w* in center and whole model in thermostat with the bottom layer of atoms fixed. In order to reduce the GB surface tension, lattice 1 will start to grow and lattice 2 shrinks. The rate of change of area of half-loop lattice 2 (Figure 2.8) is proportional to the reduced mobility as mentioned in Eq.2.9.

Their results support the corresponding experimental results that the GB velocity is proportional to the curvature and its temperature dependence obeys Arrhenius Equation (Eq.2.7) from which the activation energy of GB migration could be extracted. A tiny deviation in the activation energy between experimental method and this simulation is probably due to (1) sufficient

impurities exist in real material in experiment rather than during simulation (2) the simulation is two dimensional rather than three dimensional in experiment (3) Lennard-Jones potential is not adequate.

This image has been removed due to copyright issues. Please refer to its source.

Figure 2.7 The simulation cell in X-Y plane depicting the symmetrical U-shaped half loop GB (width *w* and misorientation angle 30˚). The bottom 3 layers of atoms are frozen at 0 K and the remaining atoms are thermostated to the desired temperature[11]

This image has been removed due to copyright issues. Please refer to its source.

Figure 2.8 The time dependence of the area of U-shaped half-loop grain 2 as the GB migrates for the simulation depicted in Fig. 2.7 [11]

2.3.2.2 Thermal Fluctuation Method

Although external driving force is commonly applied to extract GB mobility, this method has its essential drawbacks. (1) As the equation 2.9 shows, only the reduced GB mobility M^* could be extracted rather than intrinsic mobility by applying a driving force. (2) A curved GB which is the most frequently used and relatively accurate method to generate a driving force still has problems. Since a curvature has tangents with different directions at different sections, the mobility vector at different sections do not have identical orientations. Thus the mobility value calculated from a curved GB could only represent an average instead of its intrinsic value[35]. (3) It is still under argument whether the velocity have a linear relationship with applied driving force especially when the driving force is small[7]. $v = p^n$ is another assumption of the relation between the driving force and the velocity of GB migration put forward by Dr. Rath[36]. (4) Since MD simulations are limited in tens of nanoseconds, the driving force need to be very large in order to get a statistically appreciable interface migration within a short time interval. Driving force applied in simulation method (~10^8Pa) [37–39] could be several orders of magnitude higher than experimental values (10^2~10^6Pa) [7]. It has been argued [8] that such high driving

forces used in MD simulation might lead to inaccurate values of mobility by enabling unrealistically fast GB migration that can no longer be described by Equation 2.8. In this case, applying a driving force may make the results artificially higher than the intrinsic value.

IRWalk method[8] developed by Dr. Trautt et al. is to describe the thermal behavior of GB excluding any external driving forces. Their bi-crystal model is shown in Figure 2.9 with two Al ⟨111⟩ 38.2˚ tilt symmetric GBs fluctuating under a high temperature (T~0.9T_m, T_m is melting temperature of Al). The average GB positions $\bar{h}(t)$ are determined from the height profiles $\bar{h}(\boldsymbol{r}, t)$ in multiple simulations in parallel (same model and condition but only different in initial velocities,$\boldsymbol{v_0}$). The frequency of different $\bar{h}(t)$ is plotted in Figure 2.10 which obeys a Gaussian distribution:

$$f(x, \mu, \sigma) = \frac{1}{\sigma\sqrt{2\pi}} e^{-\frac{(x-\mu)^2}{2\sigma^2}} \tag{2.10}$$

where μ is the mean distribution and σ^2 is the variance distribution.

This image has been removed due to copyright issues. Please refer to its source.

Figure 2.9 Schematic of the periodic computational cell used to extract GB mobility. The two fcc crystals C($\widehat{n_1}$) and C($\widehat{n_2}$) are misoriented by tilting ⟨111⟩ crystal direction equally to Y direction. The initial position of the GB (solid unshaded planes), the fluctuating profile h(**r**, t) (shaded planes) and computed average $\bar{h}(t)$ (dotted, unshaded) are presented[8]

This image has been removed due to copyright issues. Please refer to its source.

Figure 2.10 Distribution of the average interface position $\bar{h}(t)$ at four time intervals 10ps, 20ps, 40ps and 80ps. Gaussian fits are shown[8]

This image has been removed due to copyright issues. Please refer to its source.

Figure 2.11 Linear time dependence of the variance $\langle \bar{h}^2 \rangle$. Slope is the "diffusion coefficient"[8]

With a comparison of the average interface distribution at different time intervals, the variance of the distributions $< \overline{h^2} >$ is found to have a linear proportional relationship with time as shown in Figure 2.11 while the mean value of distribution $< \bar{h} >$ is unchanged

$$< \overline{h^2} >= Dt \tag{2.11}$$

here *D* is the slope in Figure 2.11 and also known as "diffusion coefficient". Since the parameter *D* is to describe the migration of GB rather than individual atomic diffusion, it cannot be physically equal to the diffusion coefficient for atoms but mathematically could.

IRWalk behavior could be correlated with the mobility of GB migration. The velocity *v* of a fluctuating GB is due to the capillary driving forces κ_Υ and bulk Langevin force η associated with the intrinsic thermal fluctuations[40],

$$v = M(\kappa_\Upsilon + \eta) \tag{2.12}$$

The capillary force is the product of average interface curvature and its stiffness, $\kappa_\Upsilon = \kappa\Gamma$. The bulk Langevin force η due to thermal noise is expected to be independent with space and time. Then it is assumed that the interface fluctuates in a small range and small slope approximation ($\frac{\partial h}{\partial x} \ll 1, \frac{\partial h}{\partial y} \ll 1$),

$$v = \frac{\partial h}{\partial t} = M[\Gamma(\frac{\partial^2 h}{\partial x^2} + \frac{\partial^2 h}{\partial y^2}) + \eta] \tag{2.13}$$

Integrating both sides of this equation in space and time and yielding mean square displacement $< \overline{h^2} >= Dt$,

$$D = \frac{2Mk_BT}{A} \tag{2.14}$$

where A is the area of the GB plane.

Dr. Trautt, al. have also verified their results in different metals by IRWalk method. The results are generally more comparable with previous experimental data than those extracted by applying an external driving force. However, random walk results still have approximately one order of magnitude higher than experimental results which owns to the dramatic impurity drag effect in natural crystalline materials.

2.4 Triple Junction

As the conjunction of three GBs, TJ is a one-dimensional defect which is considered to present extreme disordered and open structure. Its properties and structures depend closely on the three adjacent GBs. Thus, TJ could be classified into three types[41]: general TJ connecting three general GBs, mixed TJ connecting general & special GBs and special TJ connecting three special GBs (see Figure 2.12).

This image has been removed due to copyright issues. Please refer to its source.

Figure 2.12 Different types of TJs consist with (a) three general GBs; (b)(c) mixed GBs and (d) three coincident (special) GBs[41]

If three GBs are all coincidence (special) GBs connected with the TJ, their Σ value should have a relation[42]

$$\Sigma_1 \cdot \Sigma_2 = d^2 \Sigma_3 \tag{2.15}$$

d is an integral divisor. For instance, if two GBs are Σ=3 and Σ=9, the other one may be 3 or 9 depending on the value of d=1 or 3. Here the "special TJ" is restrictively defined since other conceptions need to be considered such as the identical GB rotation axis and GB plane orientations.

This image has been removed due to copyright issues. Please refer to its source.

Figure 2.13 Symmetric structure in TJ. Empty circle, solid circle and empty square represent atoms in three different grains solid line are the crystal planes (100), (110) and (010)[42]

A symmetric structure[42] also exists in TJ structure similar to that in GB. However, the definition differs from that of GB. A symmetric GB means the same direction in both of the grains own an identical tilt angle to the GB plane. In TJ, the symmetry is shown in Figure 2.13. If the atoms in each grain are extended to the other two grains, the TJ will be a coincidence site. Besides, each of two grains are symmetric tilt to one direction in the third grain. Thus, atoms in either grain will be coincident with one of the rest grain with a 30˚rotation.

TJ reaches to equilibrium state when the energy of three GBs is given by Young-Dupre equation[43]:

$$\frac{\gamma_1}{\sin\alpha_1} = \frac{\gamma_2}{\sin\alpha_2} = \frac{\gamma_3}{\sin\alpha_3} \tag{2.16}$$

Here γ are the energy of GBs and α are the dihedral angles between each two GBs. Figure 2.14 schematically shows the relation between these parameters. However, many experimental evidences[42] do not present exactly this relation (Eq. 2.16). The effect of torque between GBs and the present of defects in GBs should be taken into consideration. Thus, equation 2.16 is limited only to describe the general GBs which do not have a dramatic change respect to misorientation[42].

This image has been removed due to copyright issues. Please refer to its source.

Figure 2.14 Schematic description of Young-Dupre equation[42]

Dr. Gottstein et al.[44,45] provide a method to measure the triple line energy by considering the equilibrium of four tensions at TJ. As Figure 2.15 shows, three thermal grooves are created by electropolishing, heat treatment and annealing. The equilibrium state is given by[45]:

$$\gamma_{TJ}^{l} = \gamma_{1-2}^{lS} \sin \xi_{1-2} + \gamma_{1-3}^{lS} \sin \xi_{1-3} + \gamma_{2-3}^{lS} \sin \xi_{2-3} \tag{2.17}$$

Here γ_{TJ}^{l} is the triple line energy, γ_{i-j}^{lS} is the GBs energy and ξ is the angle between curved GB groove and TJ line. The geometry is observed under AFM thus all these parameter could be obtained.

This image has been removed due to copyright issues. Please refer to its source.

Figure 2.15 (a) Schematic description and (b) AFM geometry of TJ and adjacent GB grooves[44,45]

Although the atomic structure in TJs is not as fully illustrated as in GBs, TJ exhibits a higher diffusivity than GB[46] and serves as preference site for impurity segregations[47]. As a result, TJ is drawing increasing attention in recent years.

2.5 Triple Junction Mobility

TJ is a one dimensional defect in polycrystalline materials where three GBs meet. Initially an acceptable viewpoint was proposed by Dr. Mullins[2] that TJ does not affect GB motion and their role in grain growth is reduced to preserve the thermodynamic equilibrium angles. Thus GB mobility is the only intrinsic parameter to control the process of grain growth and has drawn majority of the attention. This owns to a small volume portion of TJ in regular polycrystalline materials. When the grain size is reduced to nanoscale (<100 nm), the amount of TJs could increase dramatically and comparable in order of magnitude with GBs. As a result, TJs could

play an important role or even dominate the process of grain growth in some situations. Thus, TJ mobility needs to be extracted in order to clearly present its influence on grain growth.

As similar to GB motion, TJ motion can be describe by Equation2.18[46,48].

$$v_{TJ} = M_{TJ} \cdot P \tag{2.18}$$

where M_{TJ} is TJ intrinsic mobility and P is applied driving force. However, it needs to be mentioned that TJ mobility is to describe the intrinsic property of the interface and correlated with temperature and the adjacent grains rather than applied driving force[46,48].

2.5.1 Analytical Models

A steady-state motion of a GB system with a TJ is necessary to extract the TJ mobility experimentally by applying a driving force. Up to date, a curved GB system[49] is widely used as shown in Figure 2.16 (a), which is a very small set of geometrical boundary configurations. It could be possibly assumed in this structure that the curved GBs maintain their shapes during migration so that the entire system move with a constant velocity V. the parabolic boundary shape is symmetric to x axis so only half of the curve need to be determined[49], e.g., GB I

$$y(x) = \xi \arccos\left(e^{-\frac{x}{\xi}+C_1}\right) + C_2 \tag{2.19}$$

$$\xi = \frac{a}{2\theta}\,, C_1 = \frac{1}{2}\ln(sin\,\theta)^2\,, C_2 = \xi(\frac{\pi}{2} - \theta) \tag{2.20}$$

Boundary condition is $y(0) = 0, y(\infty) = \frac{a}{2}, y'(0) = \tan\theta$

This image has been removed due to copyright issues. Please refer to its source.

Figure 2.16 Geometry of the GB system with TJ during steady-state motion (a) $\theta < {}^{\pi}/_{3}$ (b) $\theta > {}^{\pi}/_{3}$ [49]

The steady-state velocity V is found by Dr. Galina et al.[50]

$$V = \frac{2\theta m_b \sigma}{a} \tag{2.21}$$

where σ is the GB surface tension. θ in this structure is refined smaller than $\pi/3$.

The normal GB displacement rate *v* is equal to

$$v = \sigma m_b K \tag{2.22}$$

K is the local curvature of the GB

$$K = \frac{d\varphi}{dl} = -\frac{y''}{[1 + (y')^2]^{\frac{3}{2}}} \tag{2.23}$$

φ is the tangential angle at any given point of GB. During the steady-state migration, the velocity *V* parallel to x axis is related to the rate of normal displacement *v*

$$v = V\cos\varphi = V\frac{y'}{[1 + (y')^2]^{1/2}} \tag{2.24}$$

From Equations 2.22, 2.23, 2.24, the second-order differential y'' could be

$$y'' = -\frac{V}{m_b \sigma} y'[1 + (y')^2] \tag{2.25}$$

In Dr. Protasova et al. work[49], they assumed that all GBs possess identical properties irrespective of GB misorientation and crystallographic orientation. In this case, a driving force $\sigma(2cos\theta - 1)$ act on the TJ, its velocity will be

$$V = m_{tj}\sigma(2\cos\theta - 1) \tag{2.26}$$

When the system reaches to its steady state, the TJ velocity in Equation 2.26 should equal to the whole system steady-state velocity in Equation 2.21,

$$\frac{2\theta}{2\cos\theta - 1} = \frac{m_{tj}a}{m_{gb}} = \Lambda \tag{2.27}$$

Λ is defined as dimensionless TJ mobility. It should be noticed that the TJ mobility m_{tj} is of one lower spatial dimension than the GB mobility m_{gb}. Despite this kind of difference in units between TJ and GB mobility, the Equation 2.6 and 2.18 are still reconcilable since the units of driving forces applied on TJ or GB are different, J/m^3 for GB and J/m^2 for TJ, respectively. Basically the reason is that GB and TJ are 2D and 1D defects, respectively.

Λ is positively correlated with θ. If we take a first-order derivative of Λ in Eq.2.27

$$\Lambda' = \frac{2(2\cos\theta + 2\theta\sin\theta - 1)}{(2\cos\theta - 1)^2} \tag{2.28}$$

The denominator is constantly positive so only the numerator needs to be considered. Figure 2.17 shows a sketch of the function $y = 2\cos\theta + 2\theta\sin\theta - 1$ in the first quadrant of the coordinate. When θ is in a range of (0, π/3), y is constantly positive. Thus Λ is positively correlated with θ.

This image has been removed due to copyright issues. Please refer to its source.

Figure 2.17 Schematic of expression $y = 2\cos\theta + 2\theta\sin\theta - 1$ in the first quadrant of the coordinate

When Λ is infinite, the TJ mobility will be infinite and the expression $(2cos\theta - 1)$ will be zero. That means no TJ drag effect on GB exists and the dihedral angles between each two GBs will reach to their equilibrium value. This equilibrium angle satisfies $2cos\theta - 1 = 0$ then,

θ

$$\theta_{eq} = 2\theta = 2\pi/3 \tag{2.29}$$

If GB Ⅲ in Figure 2.16(a) possess different properties compared with the other two mirror symmetric GBs GB I and GB Π which is assumed by Dr. Gottstein, et al. [3],

$$\sigma_1 = \sigma_2 = \sigma \neq \sigma_3 \tag{2.30}$$

then the driving force changes to $2\sigma cos\theta - \sigma_3$, where σ is the surface tension of GB I and GB Π and σ_3 is the surface tension of GB Ⅲ. Then the TJ velocity becomes

$$V_{tj} = m_{tj}(2\sigma \cos\theta - \sigma_3) \tag{2.31}$$

And the dimensionless TJ mobility will be

$$\frac{2\theta}{2\cos\theta - {}^{\sigma_3}/_{\sigma}} = \frac{m_{tj}a}{m_{gb}} = \Lambda \tag{2.32}$$

Equilibrium dihedral angle reaches

$$\theta_{eq} = 2\arccos(\frac{\sigma_3}{2\sigma}) \tag{2.33}$$

2.5.2 Experimental

Dr. Protasova[49] measured the equilibrium dihedral angle by notches pinning the two mirror symmetric GBs to avoid the complete disappearance at T=655℃ for 5 min relaxation. Then sample was rapidly cooled down after annealing. The ratio of surface tensions of these two types of GBs could also be extracted from equilibrium angle θ_{eq} by Equation 2.33. A sketch is presented in Figure 2.18.

This image has been removed due to copyright issues. Please refer to its source.

Figure 2.18 (a) GB system with TJ. Notches are to avoid the complete disappearance of the grain adjacent with GB I and GB Π; (b) the equilibrium system after annealing at 655˚C [49]

They discovered a drastic difference[49] between the activation energy of GB and TJ migration which is shown in Figure 2.19. Compared with previous data which is represented by the dotted line, TJ could affect the GB migration strongly at low temperature and the influence could weaken gradually when the temperature increases. Therefore, there exists a temperature below which TJs govern the system motion and GBs simply follow TJ. When comparing their results on two types of structures with ⟨111⟩ tilt and ⟨110⟩ tilt GBs respectively, they found this transition temperature is verified to be correlated with the geometry of GBs but still more researches is needed to support this conclusion.

This image has been removed due to copyright issues. Please refer to its source.

Figure 2.19 Temperature dependence of TJ (●) and GB (▲) mobility in (a) 21˚⟨111⟩ and (b) 21˚ ⟨110⟩ tilt GBs. Dotted line represents the mobility of a 21˚⟨111⟩ tilt GB in Al [7] (H=1.6 eV, A_0= 10^3 m^2/s)[49]

Dr. Gottstein et al. [3] investigates the effect of TJs on grain microstructure as well as GB motion. Same parabolic model is built with a curved GB and a TJ in Figure 2.16 (a). Besides, they considered another situation in which the initial angle $\theta > \frac{\pi}{3}$ in Figure 2.16 (b).

In this case, the shape function in Eq. 2.19 changes to

$$y(x) = -\frac{x_0}{\ln \sin \theta} acrcos(e^{\left(\frac{x}{x_0}\right) \ln \sin \theta}) \tag{2.34}$$

Equation 2.27 becomes

$$\frac{\ln \sin \theta}{2 \cos \theta - 1} = \frac{m_{tj} a}{m_{gb}} = \Lambda \tag{2.35}$$

When structure in either of these two situations reaches to equilibrium, the dimensionless TJ mobility Λ will reach to infinity and no drag effect of TJ on GB migration could be detected. The

relationship between Λ and θ_{eq} is shown in Figure 2.20. The equilibrium angle will get close to and eventually equal to a specific value $\frac{\pi}{3}$ irrespective of the initial dihedral angle.

This image has been removed due to copyright issues. Please refer to its source.

Figure 2.20 Half the dihedral angle θ as a function of Λ. (a) Geometry in Fig.2.16(a); (b) geometry in Fig.2.16(b) [3]

The positions of TJ and GB are illustrated by identifying crystal orientations in these grains using Electron Back Scatter Diffraction[3,49]. An optical microscope and polarisation filter is used to measure the migration rate and geometry under a polarised light in Gottstein's work[3] while X-ray diffraction is applied to measure the geometry in Protasova's study[49]. The dihedral angle θ is observed to be pretty constant at a given temperature (see Figure 2.21) and increase with increasing temperature (see Figure 2.22). The dimensionless TJ mobility is also plotted in Figure 2.23 with temperature which shows a lower rate increasing at low temperature while a relatively higher rate increasing at high temperature. It indicates that at low temperature, the motion of the GBs is dragged by hardly mobile TJ while the TJ becomes more mobile compared with the GB as indicated by an increasing value of Λ at high temperature. Therefore the drag effect of TJ will attenuate at high temperature and the system motion is governed by GB mobility only.

This image has been removed due to copyright issues. Please refer to its source.

Figure 2.21 Reproducibility of measurement of the angle θ at five different temperatures[3]

This image has been removed due to copyright issues. Please refer to its source.

Figure 2.22 Evolution of the shape of the GB system of a sample with symmetrical TJ with increasing temperature[3]

This image has been removed due to copyright issues. Please refer to its source.

Figure 2.23 Temperature dependence of the criterion Λ for a symmetric TJ [3]

Dr. Gottstein et al. [4]also studied the influence of TJ on grain growth. The area of N-sided grains (N=2, 3, 4, 5) are plotted with the angle β (same as θ mentioned in other works) in Figure 2.24. When β increases to its equilibrium value (the interaction of every curvature with x-axis where the area shrinkage rate reaches zero), the rate of microstructure evolution during grain growth will reduce linearly.

This image has been removed due to copyright issues. Please refer to its source.

Figure 2.24 The area rate of shrinkage for 2-, 3-, 4-, 5-sided ($\beta < \pi/3$) grains as a function of critical inclination angle β. β increases with the TJ drag force[4]

2.5.3 Molecular Dynamic Simulations

Dr. Upmanyu[46] studied the TJ mobility using MD simulation which has been successfully applied to extract the GB mobility. Similarly a half-loop structure (see Figure 2.25) is built in their model. A thermodynamic driving force is given by

$$F_{TJ(s)} = \gamma_{ab_1} \cos\beta_{ab_1} + \gamma_{ab_2} \cos\beta_{ab_2} - \gamma_{b_1b_2} \tag{2.36}$$

where $\gamma_{ab_1}, \gamma_{ab_2}, \gamma_{b_{1b_2}}$ are the GB surface energy and $\beta_{ab_1}, \beta_{ab_2}$ are the included angles within grain a. $\beta_{ab_1} = \beta_{ab_2} = \beta_s$ when static equilibrium is reached and $F_{TJ(s)} = 0$. Thus

$$2\gamma \cos\beta_s = \gamma_{b_1b_2} \tag{2.37}$$

When the system hasn't reached to its equilibrium, the dynamic angle β_d is different from β_s

$$F_{TJ(d)} = 2\gamma \cos\beta_d - \gamma_{b_1b_2} = 2\gamma(\cos\beta_d - \cos\beta_s) \tag{2.38}$$

$$v_{TJ} = M_{TJ}F_{TJ(d)} = 2\gamma M_{TJ}(\cos\beta_d - \cos\beta_s) \tag{2.39}$$

$$\dot{A_{TJ}} = v_{TJ}w = 2\gamma M_{TJ}(\cos\beta_d - \cos\beta_s)w \tag{2.40}$$

Here $\dot{A_{TJ}}$ is the rate of change of area of the half-loop grain *a*.

This image has been removed due to copyright issues. Please refer to its source.

Figure 2.25 Half-loop structure in (a) tri-crystal and (b) bi-crystal in MD simulation[46]

In bi-crystal model with a half-loop shape GB, the rate of change of area

$$\dot{A_{GB}} = v_b w = M_{GB}\gamma\kappa w = \left(\frac{2M_{GB}\gamma}{w}\right)w = 2M_{GB}\gamma \tag{2.41}$$

so the dimensionless TJ mobility in simulation equals to

$$\Lambda_{sim} = \frac{M_{TJ}w}{M_{GB}} = \frac{\dot{A_{TJ}}}{\dot{A_{GB}}} = (\frac{1}{\cos\beta_d - \cos\beta_s}) \tag{2.42}$$

Compared with the analysis value using Eq. 2.21 and Eq. 2.39

$$\Lambda_{an} = \frac{M_{TJ}w}{M_{GB}} = (\frac{\beta_d}{\cos\beta_d - \cos\beta_s}) \tag{2.43}$$

Here is a big advantage of MD simulation over experimental method. The changing rate of area in grain *a* could be exactly represented by the atoms in grain *a* while it seems not possible to count atoms number and the measurement of area changing rate is not an easy job in experimental method.

When the parameters$\dot{A_{TJ}}$, $\dot{A_{GB}}$, β_d, β_s are measured and calculated in different models with a varies of grain misorientations θ[46], a comparison between Λ_{sim} and Λ_{an} in Figure 2.26 indicates a similar behavior of this two kinds of dimensionless TJ mobility, which means the only difference, the dynamic angle β_d is very close to its equilibrium value π/3 irrespective of misorientation angles. Besides, both the analysis value and simulation value reach to their minimum at some specific misorientation angles[46] (Σ=13,θ=38.2˚and Σ=7,θ=32.2˚). Although

more simulations are required in other misorientations to determine the global minimum point, the variation of Λ is not monotonic.

This image has been removed due to copyright issues. Please refer to its source.

Figure 2.26 The dimensionless TJ mobility Λ as a function of the GB misorientation θ for $w=25r_0$ and $T=0.125\varepsilon/k$ [46]

Dr. Upmanyu[46] also verified a threshold value of grain width *w* under which TJ has a drag effect. Otherwise TJ drag has little effect on grain growth kinetics. (Figure 2.27(a))

This image has been removed due to copyright issues. Please refer to its source.

Figure 2.27 (a) The migration rate of TJ v_{tj} plotted as a function of the inverse of *w*[46] (b) The dimensionless TJ mobility plotted as a function of the grain width w[48]

In another study by Dr. Upmanyu[48], TJ migration in the opposite direction is studied with the models in Figure 2.28 and the misorientation dependence of dimensionless TJ mobilities in both directions are compared in Figure 2.26 and Figure 2.29. The dimensionless TJ mobilities in both directions have some similar trends. For example, both have local minimum values at $\Sigma=7$ ($\theta=38.22^\circ$) and $\Sigma=13$ ($\theta=32.21^\circ$). In addition, the simulation value and analysis value of dimensionless TJ mobility are comparable in both directions. However, the value of TJ dimensionless mobility in the opposite direction is an order of magnitude smaller than that in the other direction.

This image has been removed due to copyright issues. Please refer to its source.

Figure 2.28 (a) and (b) are the TJ migration simulation geometries in two opposite directions (+ and -). (c) is the geometries of bi-crystal model with same curved GB[48]

In addition, the TJ dimensionless mobility is dependent on the grain width *w* in Figure 2.27 (b). When the grain size is small, the TJ dimensionless mobility is maintained at a finite low level. This indicates a dramatically high drag effect of TJ on GB migration when the grain width is

lower than 30 times the radius of atoms. This result matches pretty well with their previous studies shown in Figure 2.27 (a).

This image has been removed due to copyright issues. Please refer to its source.

Figure 2.29 misorientation dependence of the TJ dimensionless mobility in the opposite direction compared with Figure 2.26[48]

However, both experimental and simulation methods to extract the TJ mobility encounters a common problem similar to that in extracting GB mobility, the curved GB structure. Two main reasons as mentioned in GB mobility section are, (1) Applying a driving force from curved GB could artificially make the result higher than intrinsic value. The intrinsic mobility $\boldsymbol{M}$ still cannot be extracted from the reduced mobility $M^* = M\gamma$ they got. (2) The applied driving force with curved GBs is much larger than in experimental studies which could make the results artificially higher than intrinsic mobility. Thus, a compatible method which could avoid these drawbacks is necessary.

2.6 Grain Boundary Diffusion

GBs could provide easy paths for mass transport in polycrystalline materials since the energy of defect formation and migration in GBs tends to be much lower than that in the bulk lattice. Figure 2.30 is a direct evidence of the GBs diffusion dominant the penetration file over volume diffusion especially when it is far away from the surface. Kinetics of many microstructural changes such as phase transformation, solid-state reactions, recrystallization and grain growth are often controlled by GB diffusion[51,52]. Besides, GB diffusion causes nanocrystalline materials degradation by playing an important role in diffusion-dependent properties like creep, sinter, corrosion and ionic conductivity which are particularly noticeable at low temperature[6]. TJ diffusion, however, does not attract as much attention as GB diffusion initially due to its small

volume fraction in polycrystalline materials. Recently when the grain size is reduced to nanoscale (<100 nm), it has been found experimentally that diffusivity in nanocrystalline materials is of several orders of magnitude larger than in microcrystalline materials[51,53] due to an increasing volume fraction of GBs and TJs. Moreover, TJs exhibit a prior choice for short-circuit diffusion over GBs in nanocrystalline materials since the volume proportion of TJs can no longer be negligible[40,53].

This image has been removed due to copyright issues. Please refer to its source.

Figure 2.30 Schematic shape of a penetration profile in the present of GB diffusion, c is the average concentration of the diffusion and y is the penetration depth [51]

Since GB migration is at most similar to diffusion across the boundary, impurity diffusion could be correlated with GB migration given by [9,10]

$$M^{imp} = \frac{D}{2n\delta}\frac{1}{C_\infty}\frac{E^0}{(kT)^2}\left[\sinh\left(\frac{E_0}{kT}\right) - \frac{E_0}{kT}\right]^{-1} \tag{2.44}$$

$$M = \frac{1}{{}^{1}/_{M^0} + {}^{1}/_{M^{imp}}} \quad , \quad C_0 = C_\infty e^{-\frac{E^0}{kT}} \tag{2.45}$$

M^0 is the GB mobility excluding impurities; M^{imp} is the impurity mobility in GB; M is the GB mobility within impurities; n and δ are the GB site density and thickness respectively; C_∞ is the bulk impurity concentration and C_0 is the impurity concentration at GB area; E_0 is the segregation energy. Since the impurity migration dominates the GB migration in strong segregation system (e.g, Ni in Al, Au in Cu), Equation 2.44 and 2.45 correlate the GB migration M positively with the impurity diffusion in GB, D. Thus, this positive correlation is extended to apply in TJ region in this work. Compared with studying TJ mobility directly, the impurity diffusion is another proper method to study the impurity influence on TJ migration.

Similar as interface mobility, diffusion along GBs and TJs follows the Arrhenius equation

$$D_b = D_{b0} \exp(^{-Q_b}/_{RT}) \tag{2.46}$$

where D_b is the diffusion coefficient, Q_b is the activation energy of GB or TJ diffusions and D_{b0} is the pre-exponential factor. The physical meaning of D_{b0} is the diffusion coefficient of an infinitely-dilute solution.

In atomistic aspect, GB and TJ diffusion coefficient in a certain direction X is given by the Einstein's relation of random walk diffusion[40,51]

$$D_b = \frac{\langle X^2 \rangle}{2\Delta t} = \frac{\sum_i (\Delta X_i)^2}{2N\Delta t} \tag{2.47}$$

where $\langle X^2 \rangle$ is the mean square displacement of atoms in GB or TJ.

2.7 Triple Junction Diffusion

Dr. Frolov and Dr. Mishin[40] firstly applied the MD simulation to study the TJ self-diffusion. Their cylinder-like model (Figure 2.31) is constructed by a symmetric Σ5(210) [100] tilt GB and two general GBs with TJ connected in pure Cu. The whole model is relaxed at 1100K for 2ns before calculating the mean square displacement parallel to the tilt axis $\langle X^2 \rangle$ of atoms in the TJ. The results (see Figure 2.32) show that

$$D_{TJ} > D_{\Sigma 5GB} > D_{GGB} \tag{2.48}$$

at all the temperatures investigated from 700K to 1315K. Here D_{TJ} is the diffusion coefficient in TJ, while $D_{\Sigma 5GB}$ and D_{GGB} are the diffusion coefficients in Σ5 symmetric tilt GB and the other two general GBs, respectively. However, the activation energies of TJ diffusion and Σ5

symmetric tilt GB diffusion are almost the same (Q_{tj}=0.47±0.02eV, Q_{gb}=0.48±0.04eV). Both of them are smaller than the activation energy of general GB diffusion (Q_{ggb}=0.71±0.02eV).

This image has been removed due to copyright issues. Please refer to its source.

Figure 2.31 The cylinder-like model to study self-diffusion in TJ. TJ and GB region are defined by black lines [40]

This image has been removed due to copyright issues. Please refer to its source.

Figure 2.32 Arrhenius diagram of diffusion coefficients D calculated for the TJ, Σ5 GB, general GB, and liquid cooper. Experimental results for self-diffusion are shown for comparison [40]

Dr. Portavoce et al. [53]studied the contribution of TJ on the GB diffusion by finite element simulations using Fisher's model[54]. They found that TJ only affect the pre-exponential factor but have little influence on the activation energy of GB diffusion in the Arrhenius equation when the grain size is less than 40 nm (Figure 2.33). Besides, they also get a similar activation energy for diffusion along TJ and Σ5 symmetric tilt GB which agreed with the results in Dr. Mishin's work[40].

This image has been removed due to copyright issues. Please refer to its source.

Figure 2.33 D_{gb} in nanocrystalline materials without TJs (◦) and with TJs (●) ($D_{tj} = 1 \times 10^{-9} cm^2 s^{-1}$). Two dash lines are results of GB diffusion in microcrystalline materials[53]

2.8 Segregation

Nanocrystalline structure is generally unstable due to its large volume fraction of interfaces with high surface energy. Thus the grain growth is self-motivated to reduce the free energy and beneficial properties of nanocrystalline materials like hardness, corrosion etc. could be ruined. Overall, adding dopants is an accessible way to stabilize nanocrystalline structure. Dr. Foiles[55]verified that dopant atoms tend to segregate in GB rather than bulk grains due to a

lower free energy when segregation occurs at GB. In addition, GB with a large misorientation angle (low Σ) is much easier for dopants to segregate.

In contrast, studies on TJ segregation are technically limited although they have been found to be preferential sites for chemical attack[56] and electromigration damage[57] especially when the grain size reduced to nanoscale recently.

Dr. Reda studied the diffusion of Ni in Cu system with GB and TJ experimentally[58]. A Field Ion Microscope (FIM) is applied to analyze the concentration of solute Ni atoms with a time-of-flight mass spectrometer and a sensitive detector. Figure 2.34 present an experimental evidence of GB acting as a prior path for impurity diffusion.

This image has been removed due to copyright issues. Please refer to its source.

Figure 2.34 Nickel diffusion in the GB and TJ in Copper crystalline materials at different times[58]

This image has been removed due to copyright issues. Please refer to its source.

Figure 2.35 (a) Ni concentration (brightness related) in GBs and TJ at a series piece of slices perpendicular to TJ line (b) Ni concentration distribution in the GB[58]

The Ni concentration is also tracked in continuous piece of slices perpendicular to TJ line which shows a higher concentration in TJ than that in GBs (Figure 2.35). Diffusion is faster in the GB part close to the adjacent TJs than that far away from TJs.

Dr. K.M. Yin et al.[47] studied Bismuth segregation in copper experimentally using energy-dispersive X-ray spectrometry (EDX) in a transmission electron microscope (TEM). The model is built with several Σ-value GBs and TJs. Concentrations of dopant atoms both in GBs and TJs are recorded and compared in Figure 2.36 as an example. The concentration of Bi is plotted at different location along a Σ5 GB with a TJ located at the very beginning. A higher concentration

(~3 times larger) of dopant atoms is observed at TJ compared with every position in the conjunct Σ5 GB. This result indicates TJ as a preferential site of dopant Bi atoms in copper matrix which has a similar trend with the results in Dr. Reda's thesis [58]. Although more results with different solute in different solvents are required to verify this conclusion, TJ segregation is drawing more and more attentions.

This image has been removed due to copyright issues. Please refer to its source.

Figure 2.36 Concentration profile along the Σ5 GB with a TJ at the end[47]

2.9 Impurity Diffusion in Grain Boundary

Since GB and TJ are the preference sites of impurities segregation due to their relatively higher energy than in bulk crystals, impurities enrichment in GB and TJ are very common in real polycrystalline materials especially nanocrystalline materials. Hence, GB and TJ provide fast diffusion paths for impurities due to their quite open and disordered structures. In addition, impurity diffusion in GB and TJ could help to illustrate GB and TJ migration mechanisms which are essential in grain growth phenomenon. However, past studies [59–61] mainly focused on GB diffusions and impurity diffusion in triple junction does not gain enough attention. Results in previous TJ-diffusion-related studies only present the enrichment phenomenon in TJ[47,58] and TJ effect on impurity diffusion in GB[53].

Impurity diffusion in GBs could be demonstrated by tracer atoms experimentally[62,63] Recent studies[61] shows a moving GB could have a contribution on the penetration profile. When the impurity is dilute in GB, the GB migration could even dominate the impurity diffusion regardless of segregation effect. Figure 2.37 is an example in which the moving GB dominates the impurities diffusion no matter it is strongly segregating solute (Ag) or slightly segregating solute

(Au) in Copper solvent. That is also the aspect I must consider in my diffusion model in which GBs are frozen without any apparent migrations.

This image has been removed due to copyright issues. Please refer to its source.

Figure 2.37 Product of GB velocity and temperature as a function of the reserve temperature[61]

Basically the impurity atoms occupying lattice site could more or less influence the perfect crystal structures and increase the probability of vacancy and other dislocations generations. Thus the impurity diffusion is generally higher than self-diffusion in perfect crystals. However, it is sometimes not true in GB according to recent studies. Dr. Mishin et al. [51] compared the impurity (Ni, Te, Se) and self- diffusion in Ag which result in two totally different phenomenon (Se in Ag): impurity diffusion is larger at a relatively high temperature while smaller at a lower temperature (see Figure 2.38). This reverse relationship is due to a competition between two aspects. On one hand, Se is a fast diffuser in Ag system. On the other hand, Se has a strongly segregating effect. Thus, at low temperature, Se tends to form local configurations reminiscent of ordered crystalline structures.

This image has been removed due to copyright issues. Please refer to its source.

Figure 2.38 Arrhenius plots of impurity diffusions and self-diffusion in Ag GB[51]

CHAPTER 3 METHODOLOGY

3.1 Molecular Dynamics Simulation

MD simulation is a computer simulation of physical movements of atoms and molecules which are determined by numerically solving the Newton's equation of motion for a system of interacting particles in a period of time. A basic procedure of MD simulation is schematically shown in Figure 3.1. Since Newton's based on classical physics without any quantum effects, MD simulation is a very accurate approximation for a large scale of measurement including nanoparticles. Compared with other simulation methods, MD simulation could present the atomic trajectory during its simulation time interval. Since the cumulative error from each step of integration cannot be eliminated entirely, Dr. Mads R. Sϕrensen [52] points out that the major shortcoming of MD simulation is the time limitation, only a time scale of nanoseconds or less could be carried out with today's computational resources which is not sufficient for thermally activated atomic jumping at low temperature, Overall, MD simulation is still pretty accurate above intermediate temperature comparable with realistic experiments.

Figure 3.1 The simple description of the MD simulation algorithm

3.1.1 Canonical Ensemble (NVT) and Isothermal-isobaric Ensemble (NPT)

Temperature in MD simulation is very important but quilt confusing. Commonly in macro scale or daily life, the temperature involves a huge number of particles thus it is a statistical quantity which equals to the kinetic energy of the system

$$E = n\frac{k_B T}{2} \tag{3.1}$$

where *n* is the number of degrees of freedom in the system.

However in MD simulation, only a small amount of atoms are used. Thus a great piece of energy cannot be rapidly transported through. This could results in an increasing of temperature during the simulation time interval.

To remove thermal energy from the boundaries of a MD system and keep the temperature at a constant value, several methods could be used including velocity rescaling, the Nose-Hoover thermostat[64,65] etc. the Nose-Hoover thermostat introduces a new degree of freedom acting as an external thermal reservoir which could exchange the kinetic energy with the target system. Isothermal-isobaric ensemble which corresponds most closely to the laboratory conditions, has fixed values of substance (N), pressure (P) and temperature (T) while Canonical ensemble has fixed values of substance (N), volume (V) and temperature (T).

3.1.2 Embed Atom Method (EAM) Potential

EAM potential[66] file is used to generate force field in the simulation system. The total energy contains two parts: a pair potential term Φ(r) describing the electrostatic core-core repulsion and a cohesive term F_α representing the energy one core gets when it is embedded in the electron cloud. The energy of an atom *i* is given by

$$E_i = F_\alpha \left[\sum_{j \neq i} \rho_\beta (r_{ij}) \right] + \frac{1}{2} \sum_{j \neq i} \emptyset_{\alpha\beta} (r_{ij}) \qquad (3.2)$$

where ρ_β is the electron density. EAM potential, as a many-body potential due to the embedding energy term F(n), has a main advantage over two-body potentials like Lennard-Jones potential which is to describe the variation of the bond strength dependently with coordination.

3.1.3 Software

Software	Functions in simulation
LAMMPS MD Simulator package[67]	Help run MD simulations
Atomeye[68]	Visualize the model at atomic level

3.2 Models

3.2.1 The Model for Extracting TJ Mobility

Figure 3.2 was a honeycomb simulation cell with pure Nickel atoms. The size was 52.1 nm in x, 2.5 nm in y, and 44.1 nm in z, respectively, with periodic boundary conditions applied along x, y, and z directions. Two identical TJs were located in the central part with a symmetric tilt Σ5(310) GB in the middle. Here Ni Σ5 was chosen to have a general comparison with previously studies[46,48,69,70] with the same type of GB involved. Ni EAM potential[71] was used and NPT isothermal-isobaric ensemble was involved to keep thermal equilibrium state of the system at 1000K with Nose-Hoover thermostat. Each simulation ran approximately up to 1 *ns* and the thermal fluctuation of the GBs and TJs was tracked every time step (5 *fs*). According to commonly 12[69,70] to 20[72,73] simulations in previous researches to study the random walk behaviour, totally 16 independent simulations with different initial conditions were performed in this work. Nickel was selected for a comparison with a lot of previous studies on GB motion which were also based on Ni.

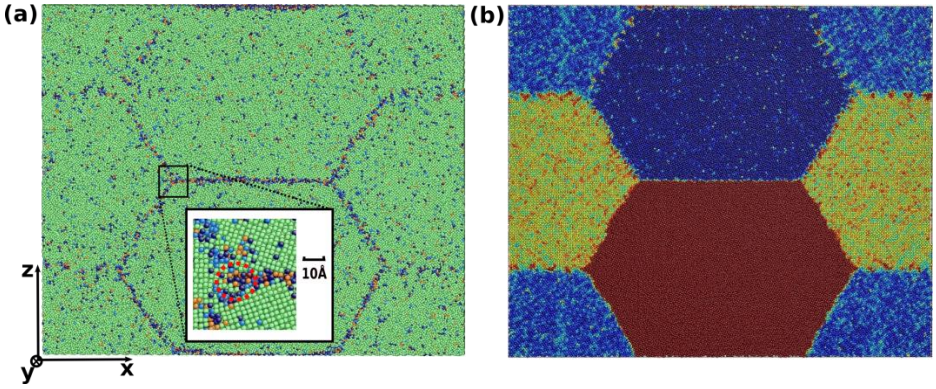

Figure 3.2 the honeycomb-shape cell in our simulation using Atomeye software. (a) Ackland parameter involved which distinguish the non-FCC atoms in interfaces from FCC atoms in the crystals. (b) Order parameter involved which distinguish atoms in different crystal grains with different orientations

3.2.1.1 IRWalk method to extract triple junction mobility

IRWalk method[8] had been applied successfully to extract GB mobility. The results agreed more closely with experimental results than that from the applied driving force method.

Since TJ is a one-dimensional defect while GB is two-dimensional, the derivation and integration process for TJ are only needed in y-direction instead of both x and y directions for GB. Thus the following expression can be derived for thermal fluctuation of TJs based on Equation 2.14:

$$D_{tj} = \frac{< \overline{r^2} >}{t} = \frac{2M_{tj}k_BT}{l} \tag{3.3}$$

here $< \overline{r^2} > = < \overline{x^2 + z^2} >$, x and z are the TJ displacement in x-z plane which is perpendicular with TJ line. ***l*** is the length of TJ. In this study, one important goal is to validate Equation 3.3.

3.2.1.2 Identification of triple junction

Two ways can be used to distinguish an interface like GB or TJ in MD simulations. One is by Ackland parameter depending on the crystalline structure and the other one is by order parameter depending on the orientations of different grains. Ackland parameter[74] distinguishes atomic structures based on the angles between bonds rather than the distance so that it is stable against temperature boost. The value of Ackland parameter 0, 1, 2, 3, 4 corresponds to the specific crystalline structures: Unknown, Body-centered cubic (BCC), Face-centered cubic (FCC), Hexagonal-close packed (HCP), Icosahedral-cluster (ICO), respectively. Thus the atoms at Ni GBs and TJs appear any number other than 2 due to their disordered structures, and accordingly TJ position can be defined as the average positions of these non-FCC atoms in TJ region.

Order parameter[38] is based on different orientations of the grains in FCC structure. An atom would have 12 nearest neighbor atoms in FCC structure which help to define the orientations

$$\xi_i = \sum_{j=1}^{12} \left| \boldsymbol{r}_j - \boldsymbol{r}_j^I \right| \tag{3.4}$$

here $\boldsymbol{r}_j^I$ is the nearest perfect lattice site of I to $\boldsymbol{r}_j$. When orientation is exactly the same as in perfect lattice I, ξ_i is then zero. When consider an atom in another lattice site with orientation J, the difference between I and J can be identified with

$$\xi_{IJ} = \sum_{j=1}^{12} \left| \boldsymbol{r}_j^J - \boldsymbol{r}_j^I \right| \tag{3.5}$$

The order parameter of atoms was generated by normalizing ξ_{IJ} into a range of (0,1). Thus, the average of the order parameter of a group of atoms in a specified region could either be certainly 0/1 when all the atoms included are from a unique grain or vary between 0 and 1 when these atoms belong to different grains, which meant GBs or TJs are covered. Due to thermal fluctuation, the order parameters lower than 0.25 or higher than 0.75 were considered to be 0 and 1, respectively in our simulations.

3.2.1.3 Four methods to track TJ displacement

Method 1: Calculation from individual GB displacement (order parameter involved)

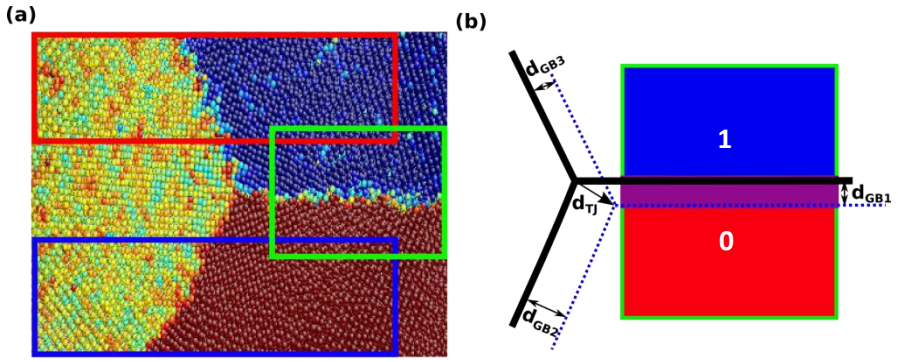

Figure 3.3 A schematic description of method 1. (a) The TJ region and three adjacent GBs; different colors represent different grains. Rectangles are three defined regions across these GBs to calculate the migration of GBs. (b) The schematic description of (a); solid lines are GBs initially and dash lines are their positions after simulation for a time period Δt. "*d*" with different subscripts indicate the displacement of TJ and GBs. Blue region in the rectangle is a group of atoms with one reference orientation and red is another group of atoms with the other reference orientation. Purple represents the atoms initially belong to reference 1 and after Δt belong to reference 0.

This was a rough approach to track the TJ displacement due to a rough assumption that no GB rotation and bending occur so that the TJ remains its equilibrium structure during the thermal fluctuations, e.g., the dihedral angles between three GBs remain at 120˚ during the simulation. In this case the TJ displacement along x and z directions were given by

$$d_{TJ,x} = \frac{d_{GB1} - d_{GB2}}{\sqrt{3}}, \quad d_{TJ,z} = d_{GB3} \tag{3.6}$$

respectively. d_{GB1}, d_{GB2} and d_{GB3} were the normal displacement of the three GBs as shown in Figure 3.3. GBs displacements could be determined by order parameter: two reference orientations were set to be 0 and 1 in each grain adjacent to the GB and a rectangular region containing a group of mixed atoms from two grains would have an average order parameter value which depends on the portion of atoms from two grains correlated with the position of GB.

Method 2: Direct detection of TJ motion (order parameter involved)

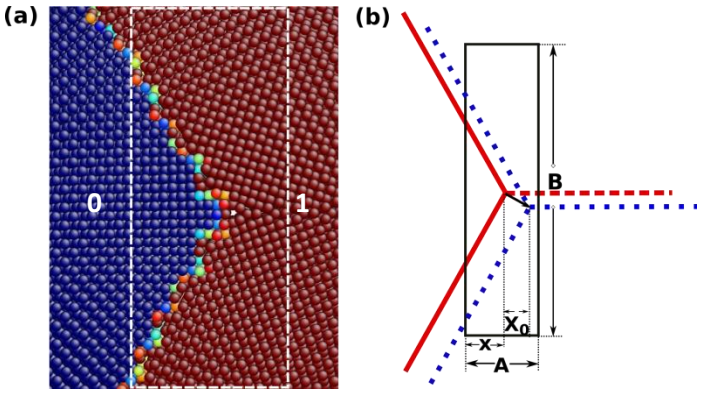

Figure 3.4 A schematic description of method 2. (a) The TJ region with three adjacent GBs; order parameter is involved. One grain is set as reference 0 while the other two grains are set as reference 1. White rectangular region is defined to calculate the TJ displacement in the horizontal direction. (b) The schematic description of (a); A and B are the length and width of the defined region. x is the height of the triangular shape in which atoms have an order parameter 0. X_0 is the TJ displacement in horizontal direction

Compared with Method 1, the TJ displacement was directly tracked in Method 2 rather than calculated from GBs displacements. However, there was still one challenge before applying this method. For instance, the increase or decrease of order parameter is enough to describe GB motion correspondingly to grain 0 or grain 1. But TJ motion is related to three grains (grain 0, grain 0.5 and grain 1) and cannot be simply identified with an increase or decrease of order parameter. Thus the TJ motion was divided to three directions in Method 2. In each direction as described in following, order parameter was able to describe the TJ motion. TJ motions in three directions could be combined together finally.

In this method, the order parameter of atoms in one grain was set as reference 0 and the other two grains were approximately set as reference 1. Figure 3.4 is one example to calculate TJ along the direction parallel to GB1 (the x direction). A sufficient long region including a triangle group of 0-value atoms and rest of 1-value atoms crossing the TJ was set. The average value of this

region depending only on the TJ motion in x direction irrespective with that in z direction was given by

$$\frac{S_{\Delta}}{S_{rec}} = \frac{\sqrt{3} \cdot x^2}{A \cdot B} = 1 - n \tag{3.7}$$

where x is relative displacement of TJ, n is the average value of rectangular region, S_{Δ} and S_{rec} the areas of rectangular and triangular region, respectively. Thus the final TJ displacement was divided into three directions along each GB.

Method 3: Calculation from the average position of atoms in TJ region (Ackland parameter involved)

Since the pure Nickel atoms have a FCC crystal structure in general grains, these atoms in the interfaces could form a non-FCC structure due to the disordered arrangement. Thus the position of TJ could be equally expressed with the average position of a group of these non-FCC atoms in the TJ region. The TJ region was defined approximately by comparing the amount of non-FCC atoms in every slice with a width of 0.7 nm and extracting the position range corresponding to the maximum amount of non-FCC atoms. Since Method 3 focuses on the atoms in the TJ (Non-FCC atoms) and did not have any mathematic calculations, it could avoid deviation dramatically during quantization and approximation. Figure 3.5 showed one example to calculate the TJ displacement in the direction perpendicular to the Σ5 GB.

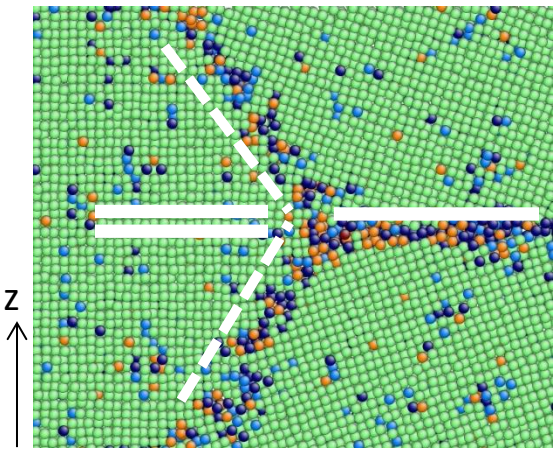

Figure 3.5 A local configuration of the TJ with Ackland parameter involved. Dash line indicates the positions of non-FCC atoms in two general GBs; solid line indicates the average position of these non-FCC atoms in z direction as well as the non-FCC atoms in the Σ5 GB which is along z direction. So the total average position of all non-FCC atoms in this region could represent the displacement of TJ in z direction

Method 4: Direct detection of TJ motion (order parameter and Ackland parameter involved)

Method 4 was an improved approach from method 3 since the TJ region was directly identified every time step. In this method, a circular region with radius of 1.2 nm moved every 0.1 nm both in x and z directions and the number of atoms belonging to grain 1, grain 2 and grain 3 in such a region were recorded as N_1, N_2 and N_3 respectively (Figure 3.6(a)). The sum of N_1, N_2 and N_3 was assumed to remain unchangeable since the area of this region was not changed. Theoretically when the circular region moved to the position at which the central point overlaps the TJ entirely, $N_1=N_2=N_3$. Thus, several mathematic relations generated at this position:

$$N_1 \cdot N_2 \cdot N_3 \rightarrow maximum$$

$$N_1^2 + N_2^2 + N_3^2 \rightarrow minimum \quad (3.8)$$

Since the assumption excluded atoms belonging to neither grains but interfaces, the second relation is more reliable to relate with TJ position (Fig. 3.6(b)). I define a new parameter N^2

$$N_1^2 + N_2^2 + N_3^2 \equiv N^2 \tag{3.9}$$

To see more clearly the minimum in the landscape, the logarithm value of N^2 was plotted inversely in Figure 3.6(c) where the peak corresponded to the position of TJ. Figure 3.6(d) was the bottom view of Figure 3.6(c) in which the TJ and GBs are clearly shown.

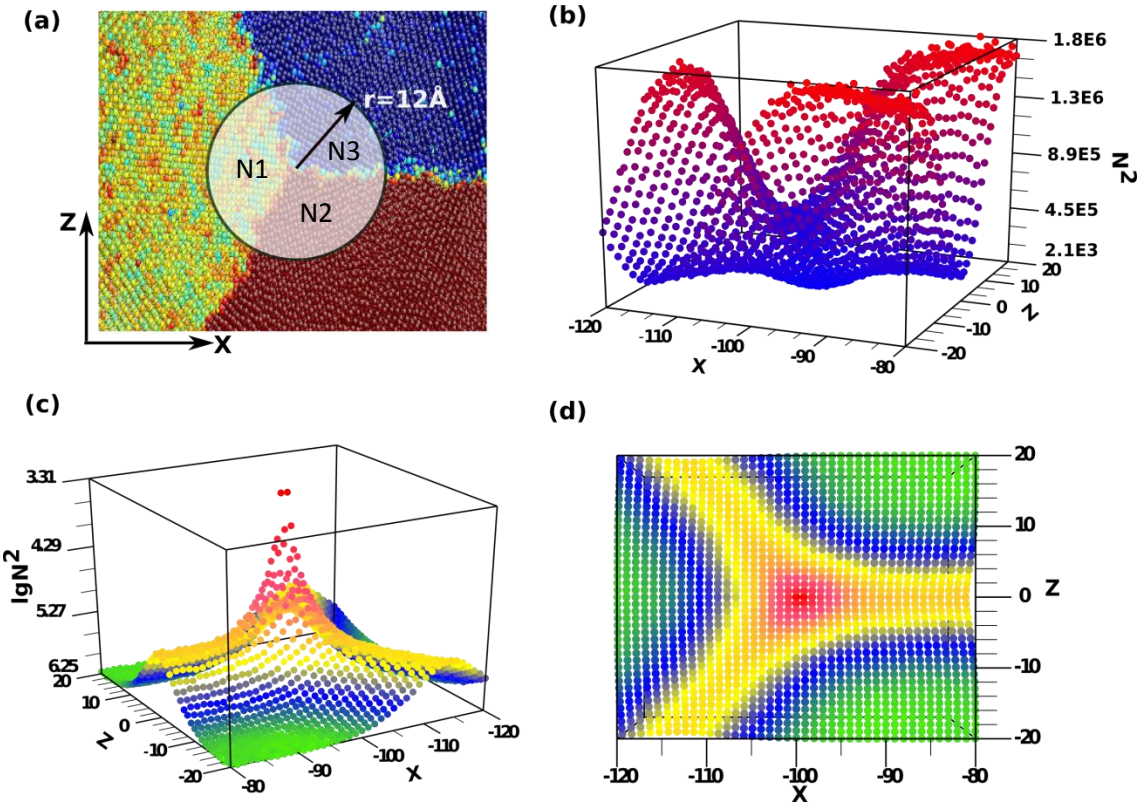

Figure 3.6 A schematic description of method 4. (a) A circular region with radius of 12Å sweeps in the x-z plane across TJ (order parameter involved). N1, N2 and N3 are the amount of atoms in this region belonging to Grain 1, Grain 2 and Grain 3, respectively. (b) N^2 calculated from Eq. 3.9 plotted in X-Z plane landscape. (c) The logarithm value of N^2 in X-Z plane landscape. (d) The view from bottom of (c)

After obtaining the position of TJ, another circular region with a radius of 0.6 nm was defined whose size was close to the size of TJ. The average position of those non-FCC atoms in this region was used as the TJ position.

3.2.2 The Model for Impurity Diffusion in Triple Junction

Figure 3.7 (a) is the model to extract the diffusivity of impurity atoms in TJ. The cell has a cylindrical shape with radius of 6 nm and length of 8 nm. Pure Aluminum atoms with Al-Ni alloy EAM potential[75] initially filled up the cell with minimized energy and Ni impurities were later added by replacing several Al atoms in the TJ region. Since the periodic boundary condition in the plane perpendicular to the tilt axis could influence the GB structure and further influence the diffusion in grain boundary during simulations[76], periodic boundary condition was only applied in y direction. After 1 ns relaxation at a raised temperature in isothermal-isobaric ensemble (NPT), atoms in the outer layer with a thickness of 1 nm were frozen and the rest atoms fluctuate under the same temperature. Different GBs type (Σ5(210) symmetric tilt, Σ5(310) symmetric tilt and Σ5 inclined tilt GBs) were studied. Temperatures from 550K to 800K with every 25K a step were considered in the simulation. At each temperature, six different concentrations of Nickel impurities: pure 0%, 0.007% (4), 0.014% (8), 0.021% (12), 0.029% (16), and 0.036% (20) (numbers in the brackets are the number of impurity Ni atoms) were studied. Mean-Square-Displacement of these impurity Ni atoms were calculated (calculate Al atoms in TJ in the pure system) under each temperature. Arrhenius relations were found and the activation energy for Ni impurities diffuse along TJ is extracted. Al is selected to study the impurity diffusion in TJ and the stabilization effect because of its inherent brittleness of GB hampering further structural application in modern industry[77]. Since Ni has a strong segregation effect in Al GB[72], it could be predicted that Ni also has a strong segregation effect in Al TJ. Thus, Ni atoms could mostly stay in TJ during simulation time and become the preference choice for me to study impurity diffusion in TJ. Most importantly, the results in this work could be compared with previous studies which focused on the diffusion of Ni impurities in Al GB[73].

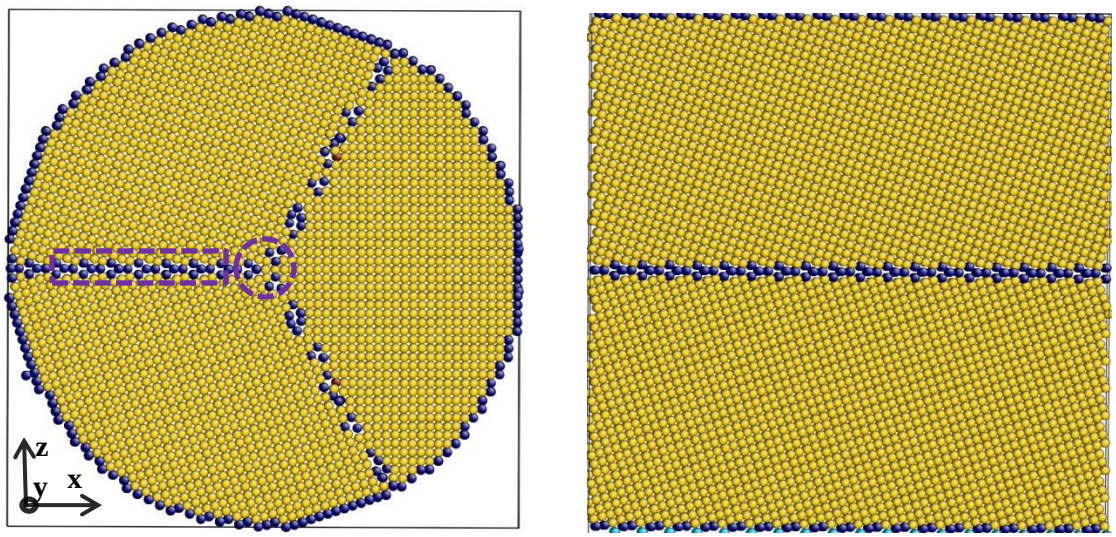

Figure 3.7 (a) A 3D cylinder model to extract the diffusion of impurity atoms in TJ. Radius is 6 nm and the length is 8 nm. A Σ5 GB (Σ5(310)[001] tilt GB in figure) is built horizontally. The circular and rectangular purple regions are defined as TJ and GB regions, respectively (b) Bi-crystal model with a specific GB (same type, same size with that in tri-crystal model) in center

As a comparison, diffusions perpendicular and parallel to the tilt axis of these three types of Σ5 GBs in bi-crystal models (Figure 3.7(b)) were studied in a range of temperature from 500K to 700K. The GB in bi-crystal models had the same size as that in tri-crystal models.

CHAPTER 4 RESULTS AND DISCUSSION

4.1 Triple Junction Mobility

4.1.1 Results from Method 1: Calculation from Individual GB Displacement (Order Parameter Involved)

Three GBs displacements and their mean square displacements are shown in Figure 4.1. The Σ5 GB shows random walk behavior as expected in Figure 4.1 (a). However, the other two general GBs do not have significant random behavior in Figure 4.1 (b) and (c). It needs to be noticed that there exists a tilt angle between the general GB and the rectangular region we defined. With the assumption that all these GBs move rigidly and the equilibrium angles between each two are $2\pi/3$, the TJ displacements in X and Z directions could be geometrically expressed with the three GBs displacements (Equation 3.6) which is shown in Figure 4.5(a).

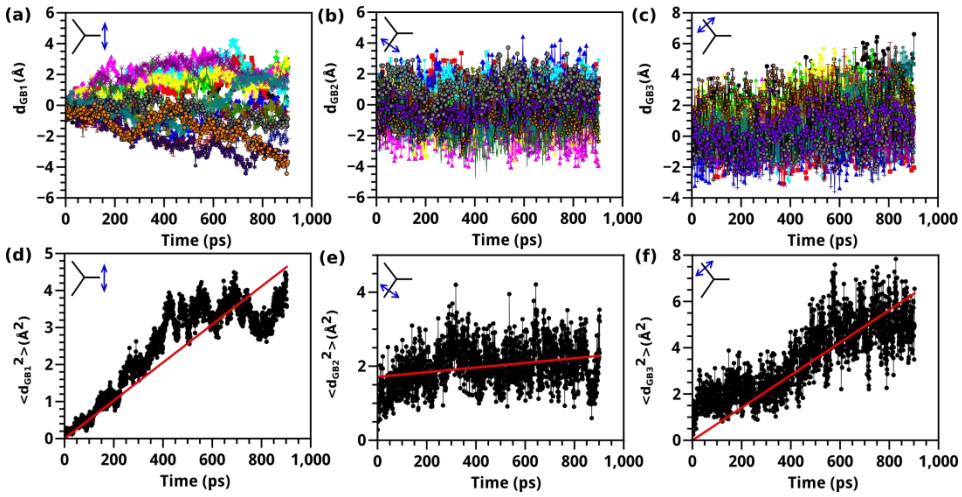

Figure 4.1 (a),(b) and (c) are the three GBs displacements in 16 random walks. (d),(e) and (f) are their corresponding mean square displacements (in Method 1)

However, this method is a rough one since the pre-assumption that the GB remains rigid during the thermal fluctuation does not hold. First of all, GB could be bent due to an asymmetric surface tension from the adjacent grains[78]. In addition, since the three GBs are not the same, the

dihedral angles could not maintain equilibrium at $2\pi/3$ as shown in Equation 2.33. Thus, this method could only provide an approximation of the TJ mobility.

4.1.2 Results from Method 2: Direct Detection of TJ Motion (Order Parameter Involved)

TJ displacements and mean square displacements in directions along three GBs are shown in Figure 4.2. TJ fluctuation in X direction (along Σ5 GB) is less dramatic than that along other two general GBs which means the stable structure of Σ5 GB could slow down TJ motion efficiently. Compared with method 1 in which whole GBs are taken into consideration, this method only focus on the TJ and a very small portion of GBs at the very end. The region defined should be long enough in the direction perpendicular to one GB so that the triangle cut by the defined region will not leak out and the shape could remain stable during the TJ fluctuation.

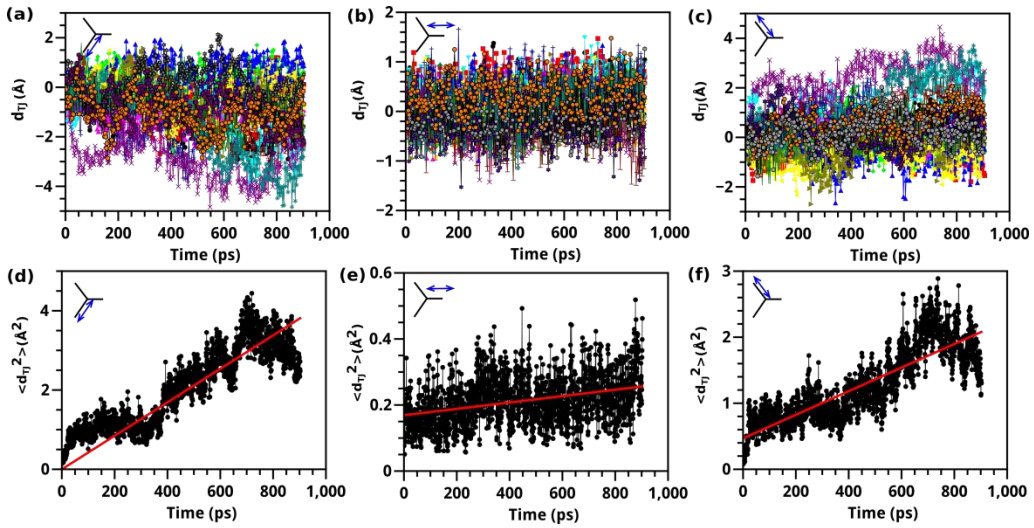

Figure 4.2 (a), (b) and (c) are TJ displacements along three GBs in 16 random walks. (d),(e) and (f) are their corresponding mean square displacements (in Method 2)

Method 2 could avoid the influence of GB bending on calculation of TJ motion. However, it is a little bit tricky in the direction along one GB (e.g. X direction in Figure 3.4). On one hand, the width of the rectangular region should be as small as possible so that only a little portion of GB is taken into consideration. On the other hand, due to TJ fluctuation, the width of the region

needs to be as large as possible to contain the TJ throughout the simulation although it has been found in method 1 that the TJ does not move a lot in X direction.

Another problem is from the order parameter. There is an approximation of order parameter due to thermal fluctuation that all values larger than 0.75 are treated as 1 and these lower than 0.25 are treated as 0. Atoms with order parameter between 0.25 and 0.75 are considered to be in GB or TJ. However, there is a considerable portion of atoms which have an order parameter between 0.25 and 0.75 especially at a high temperature in both grains due to thermal fluctuation. These atoms cannot be approximately treated as 0 or 1. For this reason, Method 2 still needs be to be improved.

4.1.3 Results from Method 3: Calculation from the Average Position of Atoms in TJ Region (Ackland Parameter Involved)

Figure 4.3 shows the TJ displacements and mean square displacements which are calculated from averaging the position of Non-FCC atoms in a defined region across TJ in three directions vertical to each GB. The TJ displacements in three directions are not so apparent as compared with the first two methods. In addition, the maximum value displacements in three directions are also 2-3 times smaller than those in first two methods. The relatively smaller displacement may be due to the large amount of non-FCC atoms taking into consideration in which a huge portion of non-FCC atoms remains stable although those non-FCC atoms in TJ move dramatically. However, Method 3 could avoid both the influence of GB bending and rotating in a small angle compared with the first two methods. In addition, the Non-FCC atoms in TJ region represent TJ directly than by identifying the three adjacent grains in first two methods.

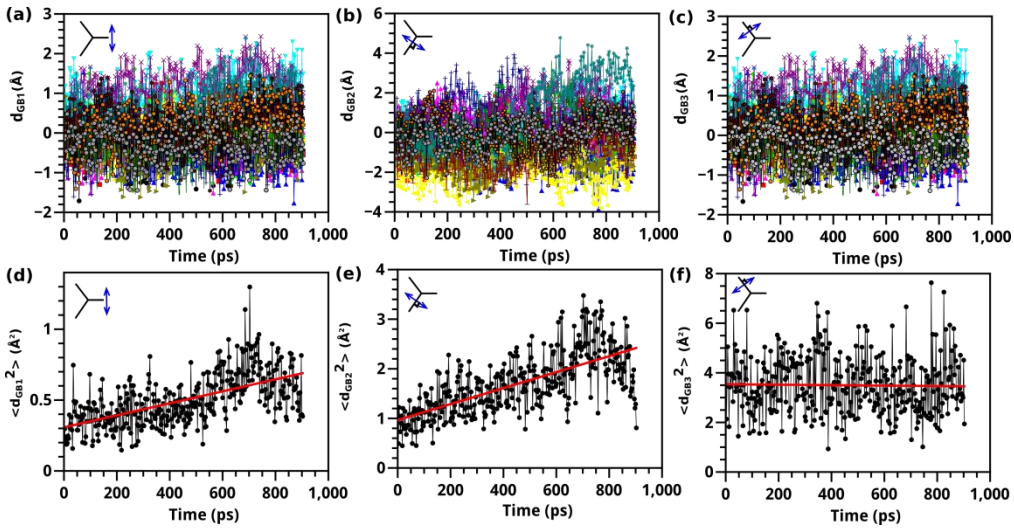

Figure 4.3 (a),(b) and (c) are TJ displacements in three directions perpendicular to each GB. (d),(e) and (f) are their corresponding mean square displacements (in Method 3)

However, same problem exist in Method 3 as in Method 2. In one hand, the defined region should be as small as possible so that the Non-FCC atoms in this region could represent TJ. In the other hand, the rectangular region must be big enough to make sure that TJ does not move out of the region during thermal fluctuation.

4.1.4 Results from Method 4: Direct Detection of TJ Motion (Order Parameter and Ackland Parameter Involved)

Figure 4.4 shows the TJ displacements and mean square displacements in X and Z directions by using Method 4. It is shown in Figure 4.4 that TJ displacement in Z direction behaves much randomly compared with that in X direction. This difference matches well with results in first three methods. As an improvement of method 3, method 4 keeps track of the approximate position of TJ before defining a region to calculate the average position of that region. This process not only helps to get the accurate value of the mobility but also reduces the error of fitting compared with method 3. The correlation coefficient R^2 representing the goodness of fit is

quite different between method 3 and method 4 in Figure 4.5 (c), (d) (R^2=0.203 in method 3, and R^2=0.707 in method 4, the closer R^2 is to *1*, the better linear fitting will be).

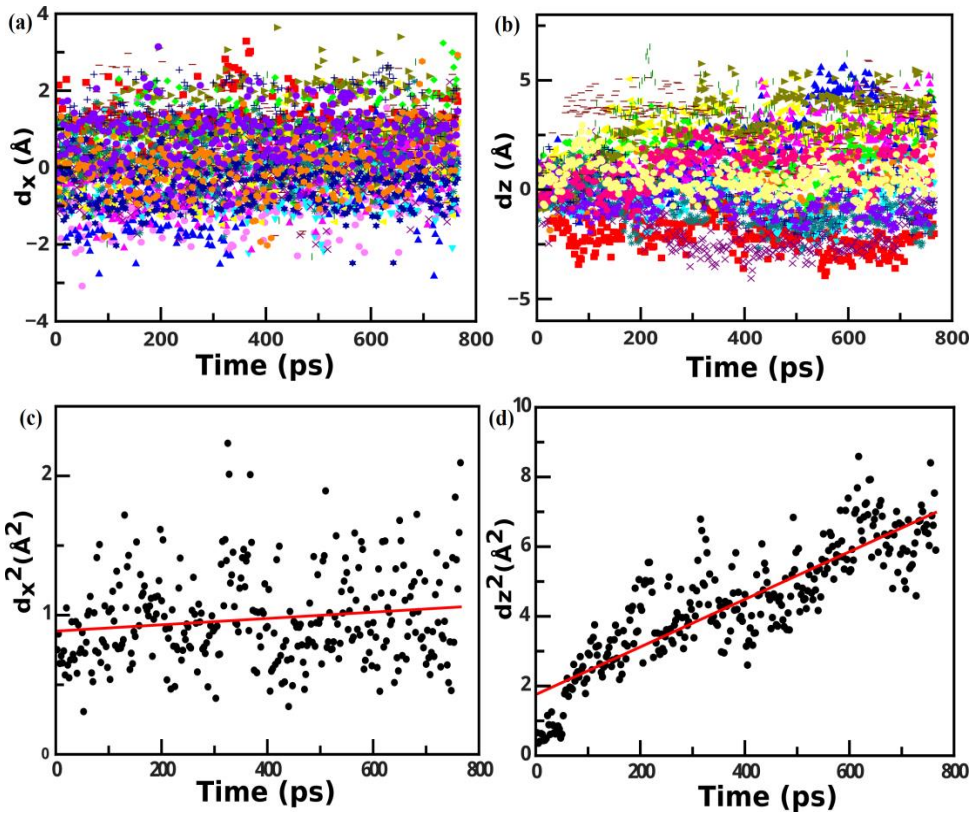

Figure 4.4 (a) and (b) are TJ displacements in X and Z direction. (c) and (d) are their corresponding mean square displacements (in Method 4)

In addition, the order parameter used in the first process in method 4 does not need to be taken into the calculation of TJ displacement. In this method, the order parameter is simply used to count the number of atoms belonging to different grains. So it avoids a mathematic approximation which could generate inaccuracy as shown in Method 1 and 2.

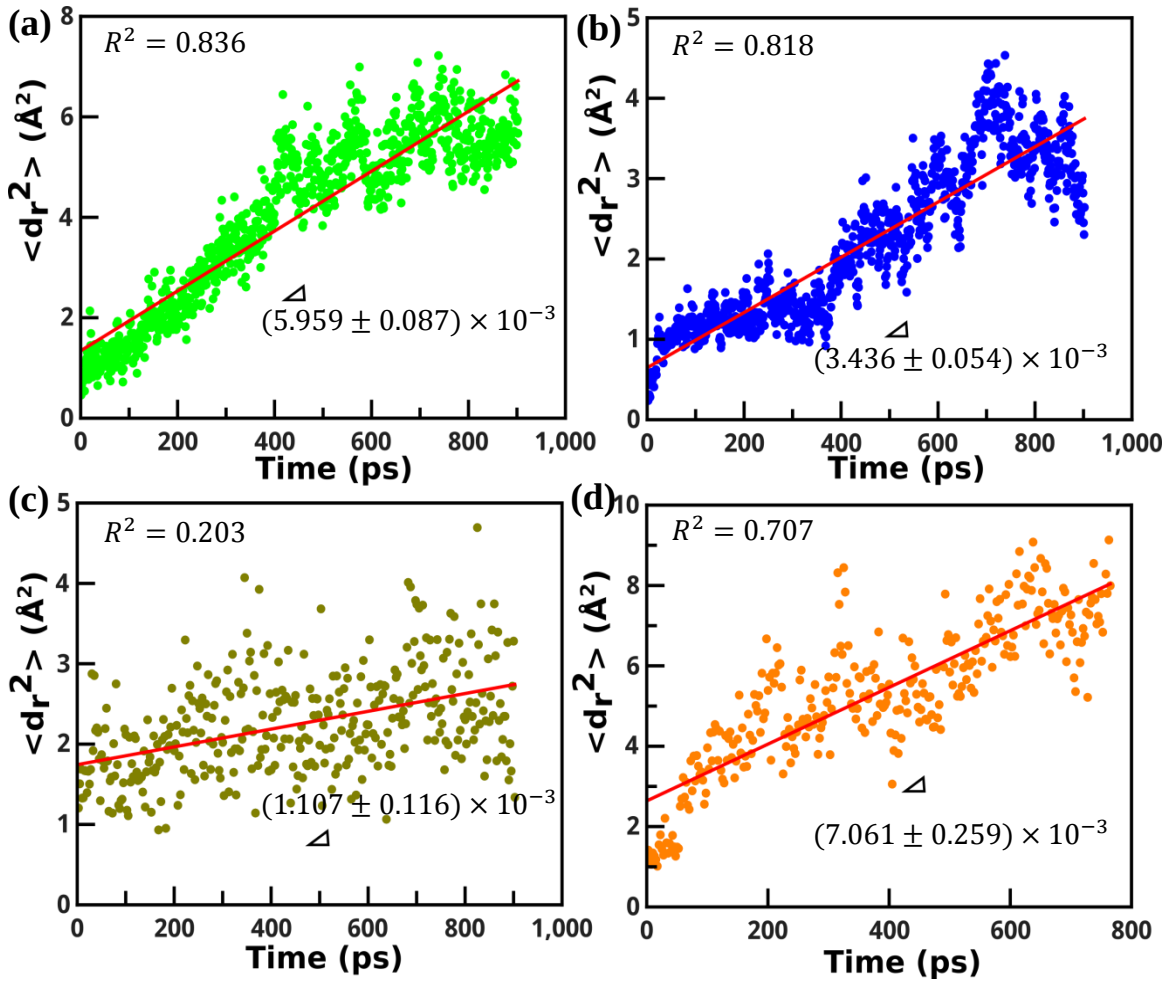

Figure 4.5 Time dependence of the mean square radius r^2 extracted from four methods (a), (b), (c) and (d), respectively. The slopes of linear fitting are the TJ "diffusion coefficient" D in Eq. 3.3. The correlation factor R^2 are shown which indicates the goodness of the linear fitting.

The parameter $\langle \overline{r^2} \rangle = \langle \overline{x^2 + z^2} \rangle$ in four methods is shown in Figure 4.5 as a function of time interval for comparison. To date, method 4 is the best one in our research and the corresponding TJ mobility is given by Equation 3.3.

$$D_{tj} = \frac{< \overline{r^2} >}{t} = \frac{2M_{tj}k_BT}{l} \tag{3.3}$$

k_B: Boltzmann Constant, $1.3806488 \times 10^{-23}\ J/K$

T: Temperature, 1000 K

l: TJ length, 2.5 nm

Since the correlation factor R^2 in Figure 4.5(d) is still low, the quality of the data needs to be improved. To achieve that, either more data points or an improved data analysis method is needed. Here an adapted data analysis is presented.

Theoretically the mean square radius is linear to time, thus a first-order equation is appropriate to describe this relationship:

$$y = at + b \tag{4.1}$$

Here a and b are the slope and intersection parameter while y stands for $\langle d^2 \rangle$. For every independent time step Δt_i (i=1,2,…n), Δy_i should be the same. Similarly, for every two time steps ($2\Delta t_i$), ($2\Delta y_i$) should also be the same, thus

$$\begin{gathered}
y(t_2) - y(t_1) = y(t_3) - y(t_2) = \cdots = y(t_n) - y(t_{n-1}) = \Delta y_1 \\
y(t_3) - y(t_1) = y(t_4) - y(t_2) = \cdots = y(t_n) - y(t_{n-2}) = \Delta y_2 \\
\cdots\ \cdots\ \cdots\ \cdots \\
y(t_{n-1}) - y(t_1) = y(t_n) - y(t_2) = \Delta y_{(n-2)} \\
y(t_n) - y(t_1) = \Delta y_{(n-1)}
\end{gathered} \tag{4.2}$$

In this case each data point in Figure 4.5(d) is inflated to be the average of (n-i) data points. After this adaption process, the correlation coefficient R^2 increases to 0.941 but the slope doesn't change too much (see Figure 4.6). This means the adaption process indeed increases the accuracy while keeps the results unchanged.

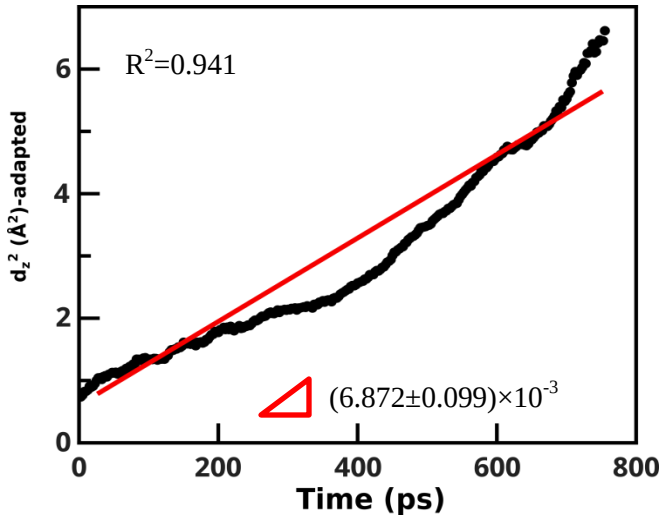

Figure 4.6 Adapted diagram from Figure 4.5(d) method 4

D_{tj} calculated from Equation 3.3 is $6.872 \times 10^{-5} \pm 0.99 \times 10^{-6} nm^2/ps$, so the TJ mobility extracted from thermal fluctuation by method 4 is

$$M_{TJ} = 6.124 \pm 0.090 \ m^3/J \cdot s \tag{4.3}$$

Notice that the above is the intrinsic TJ mobility value without applying any driving force. To justify this value, another two simulations containing the same Σ5 (310) tilt symmetric GB with the same length and boundary conditions in bi-crystal model and tri-crystal model are conducted with order parameter applied and results are shown in Figure 4.7. The Σ5 (310) tilt symmetric GB mobility are:

$$M_{GB} = 11.571 \pm 0.070 \times 10^{-8} \ m^4/J \cdot s \tag{4.4}$$

in bi-crystal model and

$$M_{GB} = 11.353 \pm 0.056 \times 10^{-8} \ m^4/J \cdot s \tag{4.5}$$

in tri-crystal model.

Consider the width of GB perpendicular to tilt axis to be 2×10^{-8} m (20nm) and the length of GB and TJ parallel to tilt axis to be the same, the mobility of TJ and that of the adjacent Σ5 (310) tilt symmetric GB are comparable (Equation 4.6).

$$\frac{M_{TJ}\cdot w}{M_{GB}}=\frac{(6.124m^3/J\cdot s)\cdot(2\times10^{-8}m)}{11.571\times10^{-8}m^4/J\cdot s}\sim1.058 \qquad (4.6)$$

The finite and comparable value of TJ mobility means at 1000K (the melting point of Ni is 1728K) in Nickel, TJ indeed has a drag effect on GB.

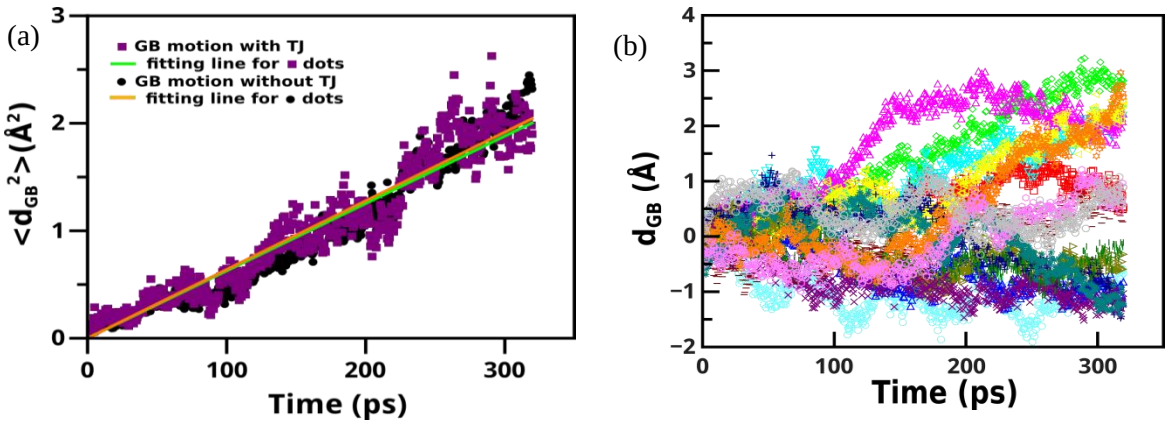

Figure 4.7 (a) Time dependence of the mean square displacement of Σ5 (310) tilt symmetric GB in both bi-crystal and tri-crystal model (b) Σ5 (310 GB displacements in bi-crystal model

By comparing TJ motion in X and Z directions (see Figure 4.8), we found that TJ migration happened dramatically in Z direction than that in X direction. This is because the Σ5 (310) tilt symmetric GB owning a lower GB energy and much stable structure could slow down the TJ migration in its direction (X).

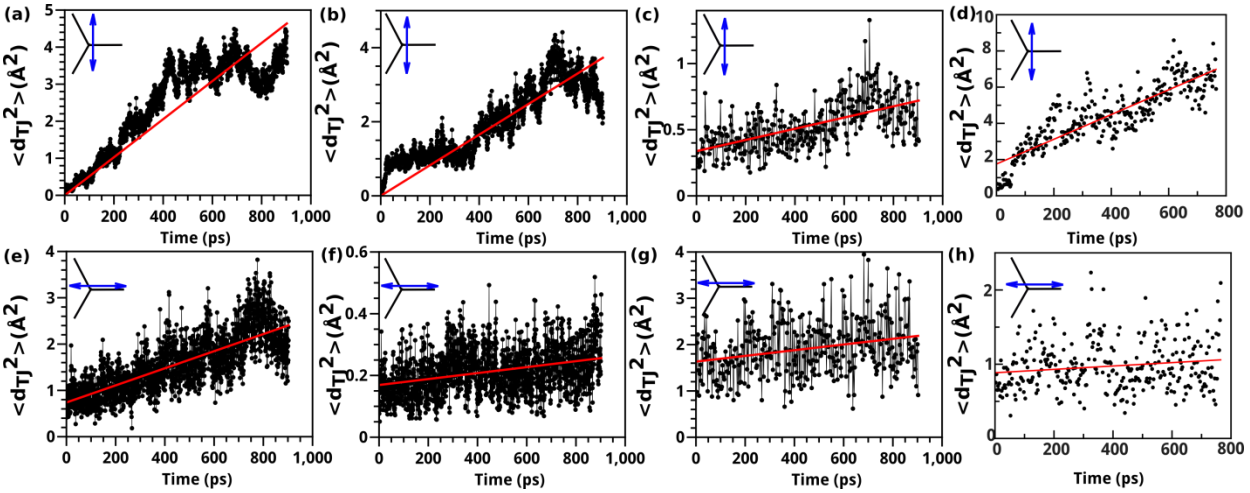

Figure 4.8 Mean square TJ displacements in Z (a~d) and X (e~h) directions extracted from method 1 (a),(e), method 2 (b),(f), method 3 (c),(g), method 4 (d),(h)

4.2 Impurity Diffusion in Triple Junction

Figure 4.9 shows the mean square displacements (MSD) in X, Y, Z directions of 12 dopant Nickel atoms in the TJ with a Σ5 (310)[001] tilt symmetric GB adjacent in pure Aluminum system at 700K (the melting point of Aluminum is 933.52K) from 16 independent simulations, among which Ydirection is the diffusion along TJ and X, Z directions are the diffusion across TJ. All of them have random-walk behaviour and diffusion in Y direction has a larger range of the mean-square-displacement.

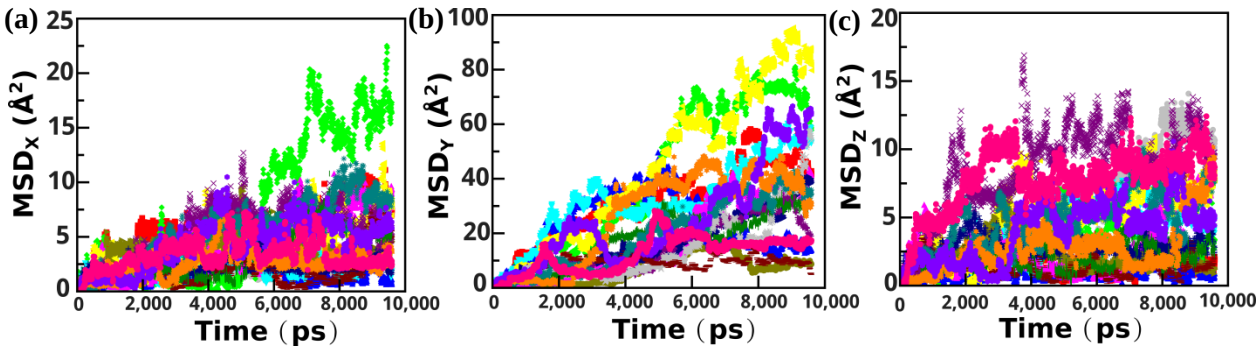

Figure 4.9 Impurity MSDs in X(a), Y(b), Z(c) directions in the TJ with a Σ5 (310)[001] tilt symmetric GB adjacent in pure Aluminum system at 700K

Taking the average value of these 16 random square displacements and doing the same process on the other simulations with 4, 8, 16 20 impurity Ni atoms in TJ, the mean square displacement could be calculated and plotted in Figure 4.10. Since the maximum global concentration of Ni atoms considered in this study is 0.036% (20 Ni atoms), or 3.9% in TJ region. we believe there is not any significant solute-solute interactions[7]. Figure 4.10 supports our prediction: there is no big difference observed among the MSD-time curvatures under different impurity concentrations. Thus, these results are equivalent and could be averaged to get the diffusion properties at a specific temperature.

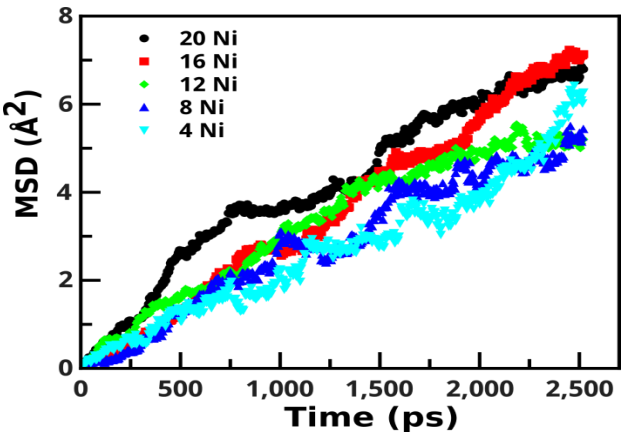

Figure 4.10 Time dependence of the impurity mean square displacements in TJ with different concentrations (number of impurity atoms) at 650K

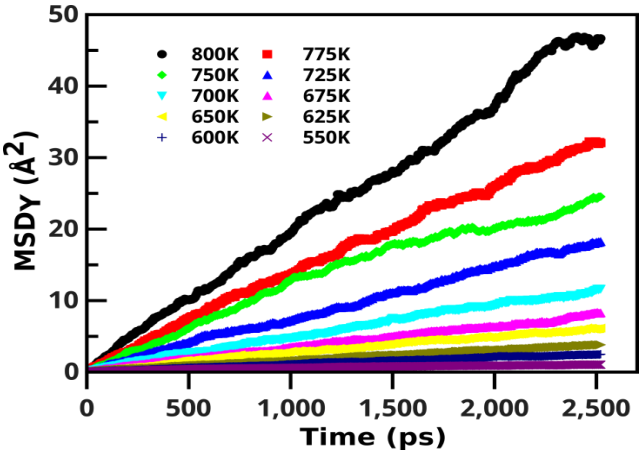

Figure 4.11 Time dependence of the impurity mean square displacement in TJ at a series of temperatures

Figure 4.11 is to show the temperature dependence of mean square displacement of the impurity diffusion in TJ. Each curvature is the average of 80 random walks simulation (16 random walks multiplying 5 impurity concentrations). The slopes of each curvature are the impurity diffusion coefficients in TJ which could be obtained by linear fitting. Obviously the diffusion coefficient increases with temperature increasing in the temperature range we studied. When the temperature is lower than 550K, the diffusion seems "frozen", which is not significant enough to be observed. When the temperature reaches 850K, the GBs and TJ could have an extremely high mobility and these impurities atoms can never catch up with. When it is higher than 850K, the interfaces begins to move away and the simulation cell structure starts to crash. In these cases, we believe the temperature range set is reasonable to study the impurity diffusion in TJ.

Figure 4.12 is then the temperature dependence of diffusion coefficients along(Y) and across(X,Z) the TJ in natural logarithm coordinate. Due to the Arrhenius relation in Equation 2.7 which could be expressed in another way

$$\ln D = -Q\left(\frac{1}{kT}\right) + \ln D_0 \tag{4.7}$$

The slope and the y-intersection of the linear fitting line in Figure 4.12 are diffusion activation energy Q and the pre-exponential factor D_0, respectively.

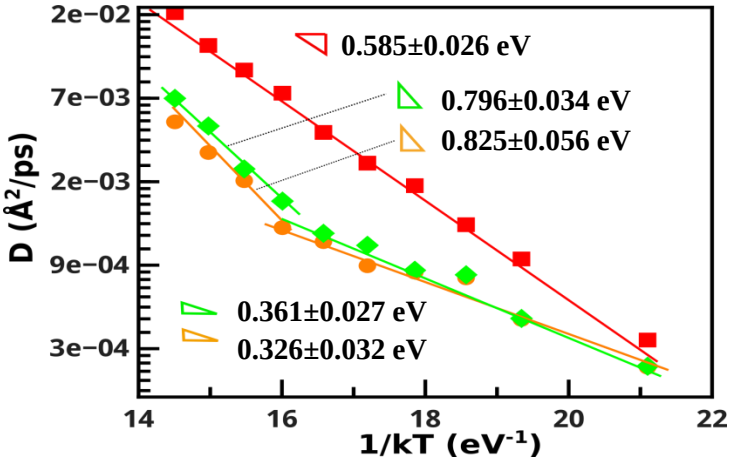

Figure 4.12 Temperature dependence of diffusion coefficients in natural logarithm coordinate along (Y in red) and across (X in green and Z in yellow) the TJ. The slope is their diffusion activation energy which are summarized in Table 4.1

It could be observed in Figure 4.12 that impurity diffusion along the TJ (Y) has a larger diffusion coefficient than that across TJ (X,Z) at any measured temperature. Difference is more significant at high temperature, nearly 3 times larger in the diffusion coefficient. We own the higher value of diffusion coefficient in Y direction to the much opened and disordered structure along TJ.

Diffusion along TJ is quite linear over the temperature range and the activation energy is 0.585±0.026eV. However, diffusion in the X and Z directions across TJ have two stages of linear relations which are different in the activation energy and pre-exponential factor (Table 4.1).

Table 4.1 the diffusion activation energy Q and pre-exponential factor D_0 in three directions X, Y, Z. Y is the direction parallel to the tilt axis.

	Activation energy, Q (eV)		Pre-exponential factor, D_0 (Å^2/ps)	
	High T (725~800K)	Low T (550~700K)	High T (725~800K)	Low T (550~700K)
X	0.796±0.034	0.361±0.027	6.545±0.534	0.588±0.500
Z	0.828±0.056	0.326±0.032	6.758±0.857	1.297±0.601
Y	0.585±0.026		4.385±0.453	

Diffusion in X and Z directions approximately have the same property on both activation energy and pre-exponential factor despite the GB geometries which is interesting.

The diffusion activation energy at high temperature is 2 to 2.5 times larger than that at low temperature in X and Z directions. It indicates that different diffusion mechanisms exist at different temperature ranges[6,52,69,70]. Since diffusion by vacancy mechanism requires extra activation energy for vacancy formation compared with diffusion by interstitial mechanism, it generally has a higher activation energy than interstitial mechanism. Thus in our results, higher activation energy at high temperature indicates diffusion by vacancy mechanism and lower activation energy at low temperature indicates diffusion by interstitial mechanism. This is reasonable because the TJ structure could be more open and disordered allowing holding more defects at a high temperature so that vacancy mechanism would dominate the diffusion process.

It should be noticed that diffusion along TJ is however dominated by one single mechanism at all temperatures. This mechanism is indicated to be the vacancy mechanism since structure along TJ is predicted to be much disordered in a long range which allows a large amount of defects exist as well. When we comparing the same mechanism in three directions, diffusion along TJ (Y) has a lower activation energy than that across TJ (X, Z).

Meanwhile, the same model with pure Al atoms was simulated to study the self-diffusion in the TJ. A Σ5 GB region 2.74 nm in length and 0.6 nm in width was defined as well as a TJ circular region with a radius of 0.5 nm (see Figure 3.7) after the core body had been relaxed for 1 ns. The sizes of the two regions were determined by visibly checking the simulation cell using Atomeye software. Not the same as in the Ni-Al system, the pure Al system could not be heated up to

800K since the triple junction would have a significant motion at around 725K. Thus, the temperature range was set from 550K to 700K. This phenomenon verifies a stabilization effect of impurities on the nanocrystalline materials, at least for Ni-Al alloy. Since the amounts of atoms studied both in GB region and TJ region were large enough to get an accurate and reliable MSD value, one random simulation was sufficient instead of sixteen. The MSD of pure Al atoms in both TJ and ∑5 GB at a range of temperature are shown in Figure 4.13 as well as the temperature dependence of diffusion coefficient in a natural logarithm coordinate. We calculate the activation energy for the ∑5 GB diffusion perpendicular to the tilt axis which is larger than that parallel to the tilt axis in ∑5 GB. This result is consistent with the research by Dr. Sϕrensen et al.[52] though the material they studied is Copper. The self-diffusion in TJ (0.572 eV) and GB (0.877eV) parallel to the tilt axis are quite different in Figure 4.13(d) as well as their diffusion coefficients magnitude. This deviation indicates that TJ is a more open structure compared with GB and holds a higher volume portion of vacancies. Compared with the Ni impurity diffusion in TJ, Al self-diffusion has a similar activation energy (0.572 eV for self-diffusion and 0.585 eV for impurity diffusion). This is interesting when we consider their same crystal FCC structure and refer to their atomic radius, 125pm for Al and 135pm for Ni[79]. Their closing atomic radius verifies Ni impurity could diffuse in Al system similar as its self-diffusion. However, situation could be different in different type of TJs which we will show later.

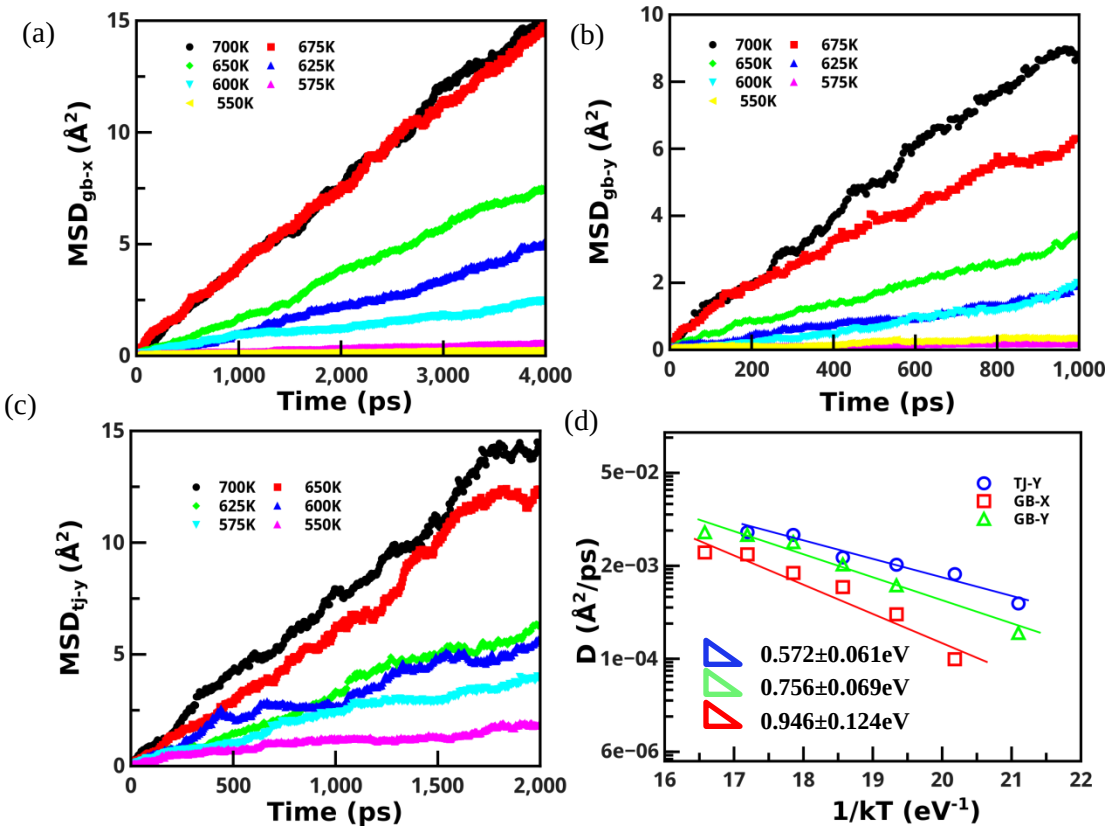

Figure 4.13 (a), (b), (c) are mean square displacements of the atoms in both TJ and ∑5 (310) tilt GB (parallel-Y and perpendicular-X to the tilt axis) in pure Al system in a range of 550K to 700K. (d)The natural logarithm value of these diffusion coefficient verse 1/kT. The activation energy are presented in (d)

In order to further compare these results, a bi-crystal model with the same ∑5 GB in identical size was simulated and results are presented in Figure 4.14. Although the model is different, these two ∑5 GBs behave similarly in the diffusion activation energy both in the directions parallel (0.756 ± 0.069eV and 0.693 ± 0.034eV) and perpendicular (0.946 ± 0.124eV and 0.868 ± 0.024eV) to the tilt axis. However the diffusion pre-exponential factors are different, which fits very well with Dr. Portavoce's results [53]. In his work, they also found that TJ could influence the GB diffusion in the pre-exponential factor rather than the activation energy. Besides, diffusion in y direction (parallel to the tilt axis) is always faster than that in x direction (perpendicular to the tilt axis).

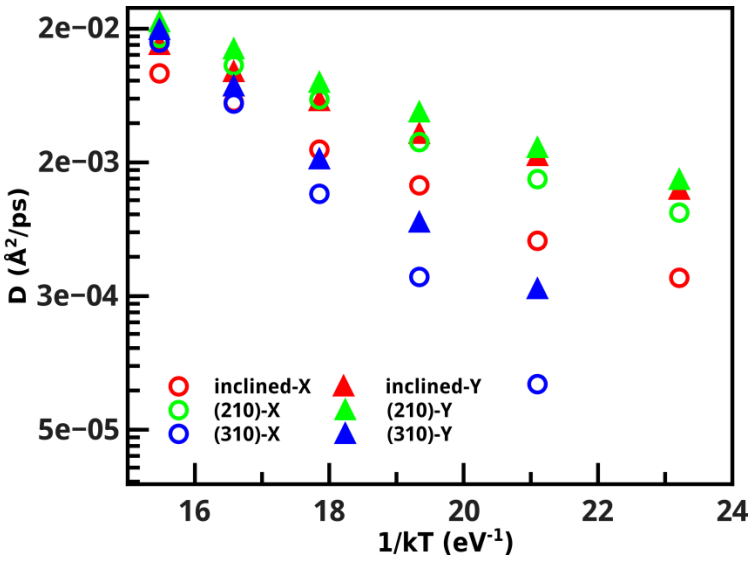

Figure 4.14 Temperature dependence of the self-diffusion coefficients in both x and y directions in symmetric ∑5(210), ∑5(310) and inclined ∑5 GBs.

In addition, we studied two other different types of ∑5 GBs, (210)[001] symmetric (53.13˚) tilt ∑5 GB and inclined ∑5 GB (53.13˚) in the same bi-crystal model, pure tri-crystal model and tri-crystal model with impurities in the TJ. Figure 4.15 and Figure 4.16 show their mean square displacements in Y direction (along TJ or parallel to the tilt axis) at a series of temperatures in tri-crystal model. Figure 4.17 is their temperature-dependence of diffusion coefficients in X (perpendicular to the GB tilt axis) and Y directions. Their diffusion activation energy and pre-exponential factors are listed in Table 4.2. Some similar trends have been found among all three ∑5 GBs. First of all, the GB diffusion perpendicular to the tilt axis always has a larger value of activation energy than that parallel to the tilt axis (an exception is the (210)[001] tilt GB in tri-crystal model). Secondly, the diffusion activation energy both in X and Y directions are very similar but the pre-exponential factor are totally different for the GB both in tri-crystal and bi-crystal model. It indicates that the TJ have little effect on the diffusion mechanism but could lead to a faster diffusion of the adjacent GB. Thirdly, the activation energy of Ni impurity diffusion in the Al TJ is comparable with that of Al self-diffusion in the TJ if we only consider the tri-crystal

system with the (210)[001] tilt and (310)[001] tilt symmetric ∑5 GBs. However in the system with the inclined ∑5 GB, they are pretty different (0.471±0.028eV for impurity diffusion and 0.336±0.023eV for self-diffusion). Last, results from ∑5 (210)[001] tilt GB system has a very close value of self-diffusion in Y direction of GB and TJ which corresponding to Mishin's study[40]. However, it is not exactly the same in the ∑5 (310[001] tilt GB systems which need to be further discussed with more data analysis.

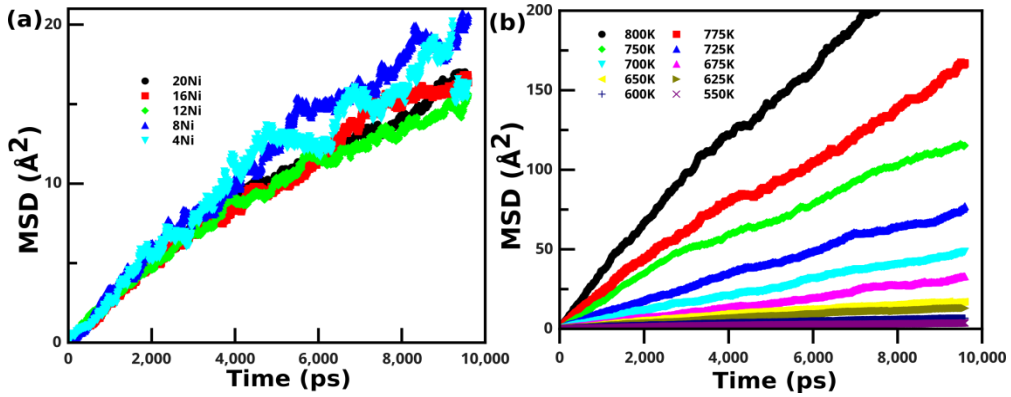

Figure 4.15 Time dependence of mean square displacements (a) of different concentrations of Ni impurities in the TJ with ∑5 (210)[001] tilt symmetric GB adjacent at 650K and (b) at a series of temperature from 550K to 800K. Curvature at 650K is the average of MSD in (a)

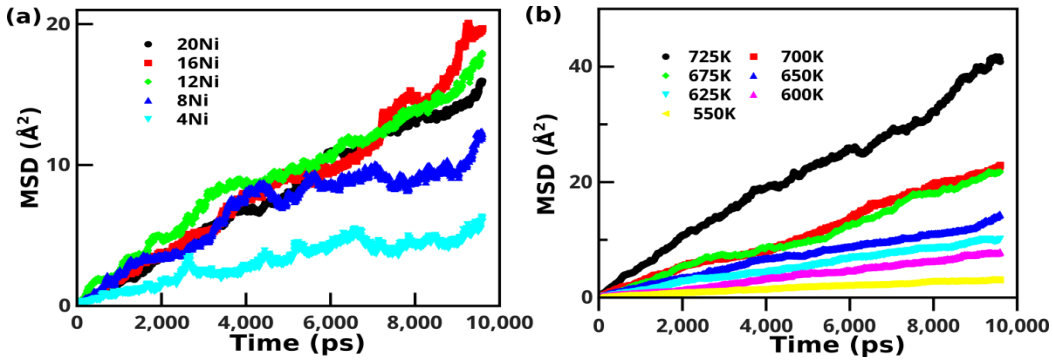

Figure 4.16 Time dependence of mean square displacements (a) of different concentrations of Ni impurities in the TJ with inclined ∑5 GB adjacent at 650K and (b) at a series of temperature from 550K to 725K. Curvature at 650K is the average of MSD in (a). The TJ structure crashed at above 750K which is then not included

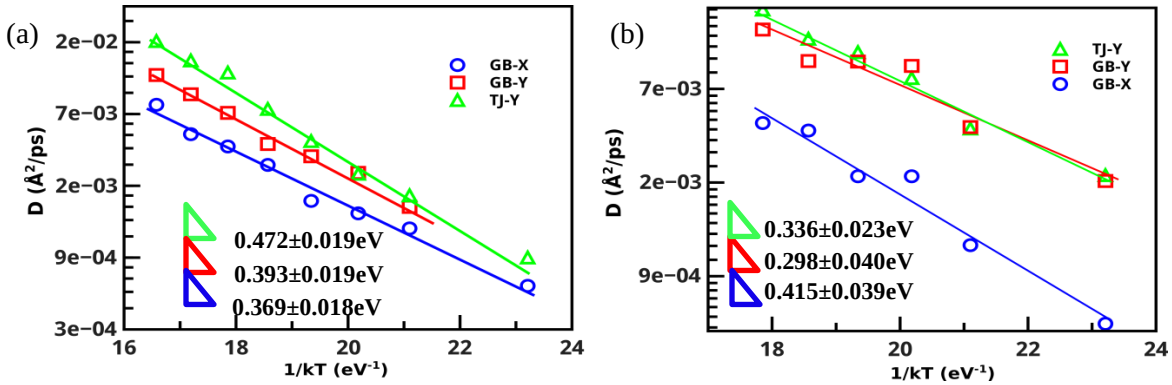

Figure 4.17 Temperature dependence of natural logarithm values of the diffusion coefficients for diffusion along TJ (Y, green), diffusion parallel to GB tilt axis (Y, red) and diffusion perpendicular to GB tilt axis (X, black) in (a) system with a ∑5 (210)[001] tilt symmetric GB, (b) system with an inclined ∑5 GB

Table 4.2 the diffusion activation energy Q and pre-exponential factor D_0 of (a) impurities diffusion in TJ, (b) self-diffusion in TJ and GB in pure Al system, and (c) self-diffusion in GB in pure bi-crystal models in directions of (i) parallel and (ii) perpendicular to the tilt axis in three systems with different types of ∑5 GBs

				Activation energy, Q (eV)	Pre-exponential factor, D_0 (Å^2/ps)
(310)[001] symmetric tilt GB system	Impurity in TJ			**0.585±0.026**	4.385±0.453
	Pure Al system	In TJ		0.572±0.061	5.044±1.170
		In GB	Y	0.756±0.069	7.960±1.285
			X	0.946±0.124	1.052±2.280
	Pure bi-crystal model	Y		0.693±0.034	6.606±0.625
		X		0.868±0.024	9.147±0.460
(210)[001] symmetric tilt GB system	Impurity in TJ			**0.523±0.072**	2.996±1.379
	Pure Al system	In TJ		0.472±0.019	3.837±0.360
		In GB	Y	0.393±0.019	2.024±0.367
			X	0.369±0.018	1.109±0.355
	Pure bi-crystal model	Y		0.307±0.015	0.758±0.278
		X		0.347±0.018	1.155±0.352
inclined GB system	Impurity in TJ			**0.471±0.028**	1.901±0.500
	Pure Al system	In TJ		0.336±0.023	1.832±0.472
		In GB	Y	0.298±0.040	0.985±0.806
			X	0.415±0.039	2.181±0.783
	Pure bi-crystal model	Y		0.277±0.017	0.062±0.317
		X		0.407±0.020	1.557±0.390

Figure 4.18 is the impurity diffusion coefficients in the three different types of TJs. It should be noticed in the TJ with (210)[001] symmetric tilt GB adjacent at above 650K, those impurities would somehow move to three adjacent GBs instead of staying in TJ. This indicates a stronger segregation effect in (210)[001] symmetric GB than in adjacent TJ at a relatively high temperature. Thus the linear fitting is only applied on the temperature below 650K.

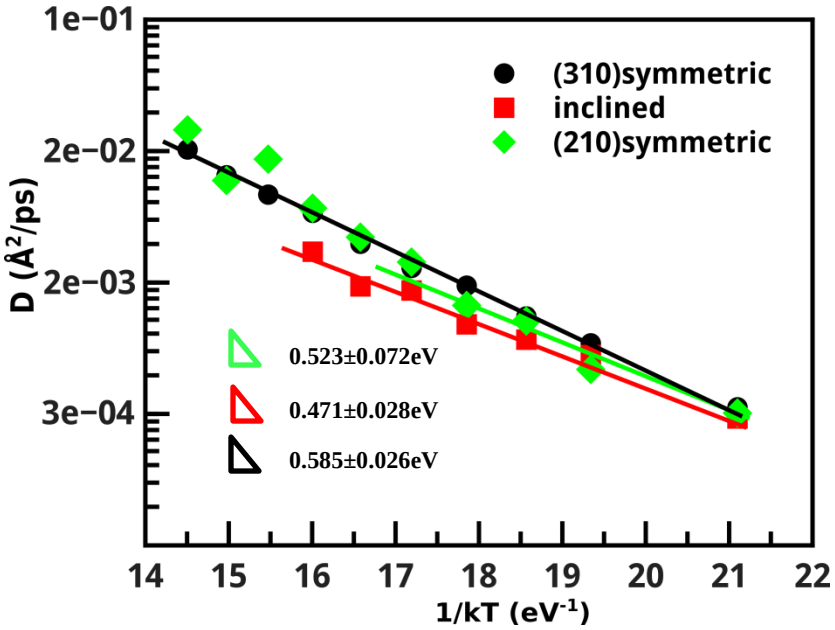

Figure 4.18 The natural logarithm values of the diffusion coefficients for the impurity diffusion along TJ with inclined ∑5, ∑5 (210)[001] tilt symmetric and ∑5 (310)[001] tilt symmetric GBs adjacent, respectively

Comparing the diffusion curvatures in Figure 4.18, the impurity diffusion in TJ does not differ much (both Q and D_0) especially at low temperatures. When the temperature rises up, generally diffusion in a TJ with symmetric GBs is a little faster but have higher diffusion activation energy than that in a TJ with asymmetric GBs even they have the same value in CSL model.

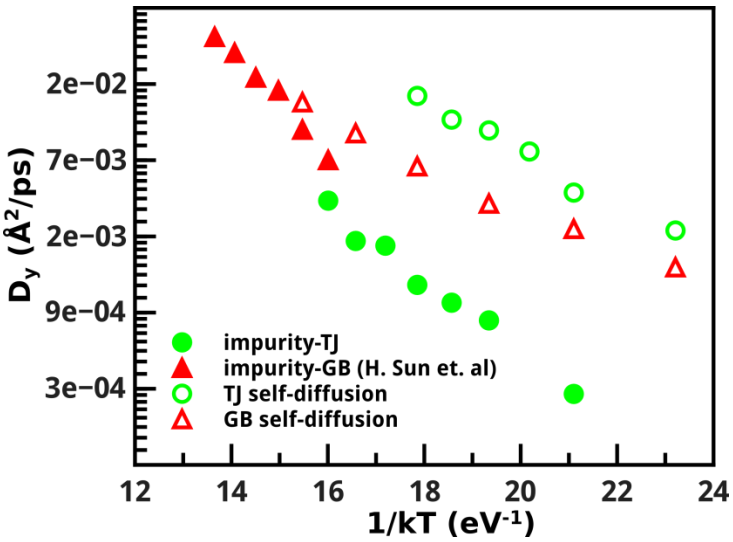

Figure 4.19 Comparison of self-diffusion and impurity diffusion both in inclined ∑5 GB and TJ with the same GB adjacent. Full red triangle data is from H. Sun[73]

In addition, the self-diffusion and impurity diffusion both in inclined ∑5 GB and TJ with the same adjacent GB are compared in Figure 4.19. Although the reference data points are in a higher range of temperature, the tendency shows that impurity diffusion has a more significant difference in TJ than that in GB with a comparison of self-diffusion. A more disordered and complicate structure is supposed to exist in TJ than that in GB.

CHAPTER 5 SUMMARY

MD simulation was performed to extract TJ mobility and impurity diffusivity in TJ. IRWalk method was applied to obtain TJ mobility while Einstein's equation was used to get the impurity diffusivity in TJ. Based on this work, six conclusions can be made as follows.

Triple junction mobility

1. The IRWalk method which has been successfully applied to extract the intrinsic GB mobility can be extended to extract the intrinsic TJ mobility: by applying order parameter and structure parameter, the triple junction position could be tracked every step so that the mean square displacement could be calculated which related with the TJ intrinsic mobility.
2. In Ni-∑5 GB system at 1000K, TJ has drag effect on ∑5 GB motion by directly comparison of TJ and ∑5 GB mobility.

Impurity diffusion in TJ with ∑5 GBs adjacent

3. The Ni impurity diffusion in Al would have similar diffusion activation energy to that of self-diffusion in the TJ region when it is adjacent to symmetric ∑5 GBs. The impurity diffusivity is independent on its concentration (when lower than 0.036%).
4. Self-diffusion at TJ and adjacent ∑5 (210) symmetric GB have similar diffusion activation energy. However, this conclusion cannot be applied to TJ-∑5 (310) symmetric GB system.
5. The similar values of ∑5 GB self-diffusion activation energy in bi-crystal model (without TJ connected) and tri-crystal model (with TJ connected) indicate that TJ would not affect the diffusion mechanism in the adjacent ∑5 GBs.

6. The difference between impurity diffusion and self-diffusion is more significant in TJ (with ∑5 inclined GB adjacent) than that in adjacent ∑5 inclined GB. This indicates a more open and complex structure in TJ (with ∑5 inclined GB adjacent) than in the ∑5 inclined GB.

Talk:

Triple Junction Mobility Extracted from Thermal Fluctuation. Materials Research Society (MRS) Spring Conference, San Francisco, California, the USA.

Future works:

1. Apply the IRWalk method to extract TJ mobility at a series of temperatures and get its activation energy
2. Study the influence of different types of impurities on the impurity diffusion in TJs within different types of GBs system (a range of misorientation angles)

REFERENCE

[1] B. Schönfelder, D. Wolf, S.R. Phillpot, Interface Sci. 5 (1997) 245.
[2] W.W. Mullins, J. Appl. Phys. 27 (1956) 900.
[3] G. Gottstein, V. Sursaeva, L.S. Shvindlerman, Interface Sci. 7 (1999) 273.
[4] G. Gottstein, A.. King, L.. Shvindlerman, Acta Mater. 48 (2000) 397.
[5] M. Chauhan, W.-A. Chiou, Y. Xun, F. Mohamed, Microsc. Microanal. 10 (2004) 658.
[6] T. Karakasidis, M. Meyer, Phys. Rev. B 55 (1997) 13853.
[7] G. Gottstein, Grain Boundary Migration in Metals: Thermodynamics, Kinetics, Applications, 2nd ed, Taylor & Francis, Boca Raton, 2010.
[8] Z.T. Trautt, M. Upmanyu, A. Karma, Science 314 (2006) 632.
[9] J.W. Cahn, Acta Metall. 10 (1962) 789.
[10] K. Lücke, H.. Stüwe, Acta Metall. 19 (1971) 1087.
[11] M. Upmanyu, W. Smith, R., D.J. Srolovitz, Interface Sci. 6 (1998) 41.
[12] M.I. Mendelev, D.J. Srolovitz, G.J. Ackland, S. Han, J. Mater. Res. 20 (2011) 208.
[13] A.D. Rollett, G. Gottstein, L.S. Shvindlerman, D.A. Molodov, Z. Für Met. 95 (2004) 226.
[14] G. Gottstein, D.A. Molodov, L.S. Shvindlerman, Interface Sci. 6 (n.d.) 7.
[15] N.J. Petch, J Iron Steel Inst Lond 173 (1953) 25.
[16] E.O. Hall, Proc. Phys. Soc. Sect. B 64 (1951) 747.
[17] C.V. Thompson, Annu. Rev. Mater. Sci. 20 (1990) 245.
[18] "Grain Boundary" Wikipedia: The Free Encyclopedia. Wikimedia Foundation, Inc., 6 Nov. 2014.
[19] W. Read, W. Shockley, Phys. Rev. 78 (1950) 275.
[20] M.A. Fortes, Phys. Status Solidi B 54 (1972) 311.
[21] M.L. Taheri, D. Molodov, G. Gottstein, A.D. Rollett, Z. Für Met. 96 (2005) 1166.
[22] F. Jensen, Qual. Reliab. Eng. Int. 1 (1985) 13.
[23] P.-L. Chen, I.-W. Chen, J. Am. Ceram. Soc. 79 (1996) 1801.
[24] M. Upmanyu, D.J. Srolovitz, L.S. Shvindlerman, G. Gottstein, Acta Mater. 47 (1999) 3901.
[25] C.A. Awo-Affouda, M.O. Bloomfield, T.S. Cale, in:, T. Grasser, S. Selberherr (Eds.), Simul. Semicond. Process. Devices 2007, Springer Vienna, Vienna, n.d., pp. 41–44.
[26] G. Gottstein, D.A. Molodov, U. Czubayko, L.S. Shvindlerman, J. Phys. IV 05 (1995) C3.
[27] P.A. Beck, P.R. Sperry, H. Hu, J. Appl. Phys. 21 (1950) 420.
[28] M. Winning, G. Gottstein, L.S. Shvindlerman, Acta Mater. 49 (2001) 211.
[29] M. Tonks, P. Millett, W. Cai, D. Wolf, Scr. Mater. 63 (2010) 1049.
[30] D.. Molodov, G. Gottstein, F. Heringhaus, L.. Shvindlerman, Acta Mater. 46 (1998) 5627.
[31] C. Capdevila, Y.L. Chen, A.R. Jones, H.K.D.H. Bhadeshia, ISIJ Int. 43 (2003) 777.
[32] B.J. Alder, T.E. Wainwright, J. Chem. Phys. 31 (1959) 459.
[33] "Molecular Dynamics" Wikipedia: The Free Encyclopedia. Wikimedia Foundation, Inc.,28 Nov. 2014.
[34] L.A. Zepeda-Ruiz, G.H. Gilmer, B. Sadigh, A. Caro, T. Oppelstrup, A.V. Hamza, Appl. Phys. Lett. 87 (2005) 231904.
[35] J.J. Hoyt, Model. Simul. Mater. Sci. Eng. 22 (2014) 033001.
[36] H. Hu, ed., The Nature and Behavior of Grain Boundaries, Springer US, Boston, MA, 1995.
[37] H. Zhang, M.I. Mendelev, D.J. Srolovitz, Acta Mater. 52 (2004) 2569.
[38] K.G.F. Janssens, D. Olmsted, E.A. Holm, S.M. Foiles, S.J. Plimpton, P.M. Derlet, Nat. Mater. 5 (2006) 124.
[39] B. Schönfelder, P. Keblinski, D. Wolf, S.R. Phillpot, Mater. Sci. Forum 294-296 (1999) 9.
[40] T. Frolov, Y. Mishin, Phys. Rev. B 79 (2009).
[41] V. Rodrigues, Triple Junctions and Low Angle Boundaries, 2006.
[42] Grain Boundaries, Springer, New York, 2012.
[43] G. Gottstein, Physical Foundations of Materials Science, 2004.

[44] G. Gottstein, L.S. Shvindlerman, B. Zhao, Scr. Mater. 62 (2010) 914.
[45] B. Zhao, J.C. Verhasselt, L.S. Shvindlerman, G. Gottstein, Acta Mater. 58 (2010) 5646.
[46] M. Upmanyu, D.J. Srolovitz, L.S. Shvindlerman, G. Gottstein, Interface Sci. 7 (1999) 307.
[47] K.M. Yin, A.H. King, T.E. Hsieh, F.R. Chen, J.J. Kai, L. Chang, Microsc Microanal 3 (1997) 417.
[48] M. Upmanyu, D.. Srolovitz, L.. Shvindlerman, G. Gottstein, Acta Mater. 50 (2002) 1405.
[49] S.. Protasova, G. Gottstein, D.. Molodov, V.. Sursaeva, L.. Shvindlerman, Acta Mater. 49 (2001) 2519.
[50] A.V. Galina, V.. Fradkov, L.S. Shvindlerman, Phys Met Met. (1987) 165.
[51] Y. Mishin, C. Herzig, Mater. Sci. Eng. A 260 (1999) 55.
[52] M. Sørensen, Y. Mishin, A. Voter, Phys. Rev. B 62 (2000) 3658.
[53] A. Portavoce, L. Chow, J. Bernardini, Appl. Phys. Lett. 96 (2010) 214102.
[54] J.C. Fisher, J. Appl. Phys. 22 (1951) 74.
[55] S. Foiles, Phys. Rev. B 40 (1989) 11502.
[56] G. Palumbo, K.T. Aust, Mater. Sci. Eng. A 113 (1989) 139.
[57] H.-U. Schreiber, Solid-State Electron. 29 (1986) 545.
[58] C.M. Reda, Atomic Transport in Nanocrystalline Materials, Doctor Thesis, University of Oran, n.d.
[59] M. Herbig, D. Raabe, Y.J. Li, P. Choi, S. Zaefferer, S. Goto, Phys. Rev. Lett. 112 (2014).
[60] C. Herzig, T. Wilger, T. Przeorski, F. Hisker, S. Divinski, Intermetallics 9 (2001) 431.
[61] C. Herzig, S.V. Divinski, Mater. Trans. 44 (2003) 14.
[62] A. Atkinson, R.I. Taylor, A.E. Hughes, Philos. Mag. A 45 (1982) 823.
[63] A. Atkinson, R.I. Taylor, Philos. Mag. A 43 (1981) 979.
[64] S. Nosé, J. Chem. Phys. 81 (1984) 511.
[65] W. Hoover, Phys. Rev. A 31 (1985) 1695.
[66] M. Daw, M. Baskes, Phys. Rev. B 29 (1984) 6443.
[67] "LAMMPS Molecular Dynamics Simulator" online available at http://lammps.sandia.gov.
[68] J. Li, Model. Simul. Mater. Sci. Eng. 11 (2003) 173.
[69] C. Deng, C.A. Schuh, Phys. Rev. B 84 (2011).
[70] C. Deng, C.A. Schuh, Phys. Rev. Lett. 106 (2011).
[71] J.E. Angelo, N.R. Moody, M.I. Baskes, Model. Simul. Mater. Sci. Eng. 3 (1995) 289.
[72] H. Sun, C. Deng, Comput. Mater. Sci. 93 (2014) 137.
[73] H. Sun, C. Deng, J. Mater. Res. 29 (2014) 1369.
[74] G. Ackland, A. Jones, Phys. Rev. B 73 (2006).
[75] G.P. Purja Pun, Y. Mishin, Philos. Mag. 89 (2009) 3245.
[76] T. Frolov, S.V. Divinski, M. Asta, Y. Mishin, Phys. Rev. Lett. 110 (2013).
[77] D. Farkas, J. Phys. Condens. Matter 12 (2000) R497.
[78] D.A. Molodov, C. Günster, G. Gottstein, L.S. Shvindlerman, Philos. Mag. 92 (2012) 4588.
[79] "Atomic radii of the elements (data page)" Wikipedia: The Free Encyclopedia. Wikimedia Foundation, Inc., 7 Dec. 2014.